Synoptic- to meso-scale atmospheric circulation connects fluvial and coastal gravel conveyors and directional deposition of coastal landforms in the Dead Sea basin

Haggai Eyal[1,2], Moshe Armon[1,3], Yehouda Enzel[1], Nadav G. Lensky[2,1]

[1]The Freddy & Nadin Herrmann Institute of Earth Sciences, The Hebrew University of Jerusalem, The Edmond J. Safra Campus, Givat Ram, Jerusalem 91904, Israel

[2]Geological Survey of Israel, 32 Yesha'yahu Leibowitz, Jerusalem 9371234, Israel

[3]Institute for Atmospheric and Climate Science, ETH Zurich, 8092 Zürich, Switzerland

Correspondence to: Haggai Eyal (haggai.eyal@mail.huji.ac.il) and Nadav G. Lensky (nadavl@gsi.gov.il)

Abstract. Streams convey coarse-clastic sediments towards coasts, where interactions with deltaic and coastal processes determine their resultant sedimentology and geomorphology. Extracting hydroclimatic signals from such environments is a desired goal, and therefore, studies commonly rely on interpreting available paleoclimatic proxy data, but the direct linking of depositional/geomorphic processes with the hydroclimate remains obscure. This is a consequence of the challenge to link processes that often are studied separately, span across large spatial and temporal scales including synoptic-scale hydroclimatic forcing, stream flows, water body hydrodynamics, fluvial and coastal sediment transport, and sedimentation. Here, we explore this chain of connected processes in the unique setting of the Dead Sea basin, where present-day hydroclimatology is tied closely with geomorphic evolution and sediment transport of streams and coasts that rapidly respond to lake-level fall. We use a five-years-long (2018-2022) rich dataset of (i) high-resolution synoptic-scale circulation patterns, (ii) continuous wind-wave and rain-floods records, and (iii) storm-scale fluvial and coastal sediment transport of 'smart' and marked boulders. We show the significance of Mediterranean cyclones in the concurrent activation of fluvial (floods) and coastal (wind-waves) sediment conveyors. These synoptic-scale patterns drive the westerlies necessary for (i) delivering the moisture across the Judean desert, which is transformed into floods, and at the same time, (ii) the coeval, topographically funneled winds that turn into surface southerlies (>10 m s^{-1}), along the Dead Sea rift valley. During winter, these meso-scale southerlies generate 10-30 high-amplitude, northward propagating storm waves, with <4 m wave heights. Such waves transport cobbles for hundreds of meters alongshore, northward and away from the supplying channel mouths. Four to nine times per winter the rainfall generated by these atmospheric patterns is capable of generating floods that reach the stream mouths, delivering poorly sorted, coarse gravels. This usually occurs during the decay of the associated storm waves. These gravels are dispersed alongshore by waves during subsequent storms. As storm waves dominate and are >five times more frequent than flash-floods, coarse-clastic beach berms and fan-deltas are deposited preferentially north of the delivering channel mouths. This asymmetric depositional architecture, controlled by the regional hydroclimatology, is identified for both the modern and Late Pleistocene coast and delta environments, implying that the dominance of present-day Mediterranean cyclones has persisted in the region also during the Late Pleistocene when Lake Lisan occupied the basin.

1. Introduction

Streams and coasts interact and convey coarse sediments. Streams deliver coarse-clastic sediments towards the coast, where the interactions with coastal processes and sediment redistribution in the basin determine deltaic and coastal geomorphology and sedimentology (Ashton et al., 2013; Galloway, 1975; Postma, 1995). While modern and Late Quaternary deltas and coasts are desired areas for settlements, agriculture, and industry (e.g., Syvitski et al., 2009), ancient deltaic and coastal successions are potential reservoirs of hydrocarbons and water (e.g., Elliot, 1986). In cases of receding water levels, when the continental shelf and/or slope are exposed, such reservoirs are formed as coarse sediments are delivered from highstand to lowstand deltas and subsequently redistributed alongshore (e.g., Blum et al., 2013) (Fig. 1).

Deltaic architecture is defined on the one hand, by the fluvial regime depending on the hinterland characteristics of the watershed, where climate generates flows carrying sediment load into basins. On the other hand, sediment redistribution and deposition are dictated by the basin's shape, size, and bathymetry, and by the hydrodynamics of waves, currents, tides, and the rate of level changes of the water body occupying the basin (see Fig. 1 in Coleman and Prior, 1982; Postma, 1990; Elliot, 1986). Nienhuis et al., (2016) suggested that channel orientation of wave-influenced deltas is preserved in the morphology of deltas and has the potential to indicate past and present fluvial and alongshore sediment transport fluxes. However, commonly the wide range of influencing factors results in diverse types of deltaic depositional configurations (Postma, 1990, 1995), from which it is challenging to decode hydroclimatic and environmental signals, even in modern environments and more so from past sedimentary records (Hansford and Plink-Björklund, 2020). Moreover, despite the importance of understanding common controls over fluvial and coastal sediment conveyors, frequently they are studied separately.

In modern *fluvial sediment conveyors*, atmospheric circulation patterns (CPs) and their association with rainfall and floods are extensively studied for specific watersheds and regions (e.g., Bárdossy and Filiz, 2005; Steirou et al., 2017; Merz et al., 2021; Kahana et al., 2002). However, linking the CPs with sediment transport is lacking. A separate body of research deals with flows in channels, their resultant bedload sediment transport (e.g., Reid et al., 1985; Wang et al., 2015; Lekach and Enzel, 2021), channel morphology (e.g., Montgomery and Buffington, 1997), and channel mouth deposition (e.g., Bridge, 1993; Wright, 1977; Coleman and Prior, 1982). In modern *coastal conveyors*, a large body of research deals with global-scale climate signals and beach change (e.g., Masselink et al., 2023). However, only a small number of studies have associated *synoptic-scale* CPs with wave climates along the shores of oceans or lakes (Pringle et al., 2014, 2015; Solari and Alonso, 2017; Graf et al., 2013), few of them attributed these processes to either longshore transport of sand (e.g., Goodwin et al., 2016) or shoreline erosion (Meadows et al., 1997; Pringle and Stretch, 2021). This small body of research stems from the complex link between synoptic-scale circulation, waves, and their resultant sediment transport; processes occurring over a wide range of spatiotemporal scales (Pringle et al., 2015, 2014, 2021; Solari and Alonso, 2017). Therefore, our knowledge regarding the joint fluvial and coastal environments is fragmented; full linking of the chain of processes/environments, from the synoptic-scale circulation conditions that generate rainstorms-floods, to wind-waves and sediment transport and deposition in each of the sediment conveyors and their interactions, is missing.

The modern Dead Sea (see regional setting in the next Sect.) is a unique environment providing a "natural laboratory" to potentially study these processes together. It has several advantages: (i) The small to medium-scale watersheds (10^1-10^3 kms) surrounding the lake (e.g., Enzel et al., 2008; Zoccatelli et al., 2019) enable studying the relative impact of different CPs on water discharge (Enzel et al., 2003; Kahana et al., 2002; Dayan and Morin, 2006) and sediment delivery to the basin (Armon et al., 2018; Ben Dor et al., 2018; Armon et al., 2019). Armon et al., (2018) have linked the rain- and flood-generating CPs and the resulting sediment plumes dispersed over the Dead Sea. Linking such sediment dispersion under the lake hydrodynamics is still missing, especially for the coarser sediments. (ii) Rapid fluvial and coastal geomorphic responses to lake-level fall enable a study of real-time geomorphic processes and present-day sedimentary accumulation under forced regression and known environmental forcing with implications to the sedimentary record (e.g., Bartov et al., 2006; Sirota et al., 2021). Focusing on gravelly sediments, Eyal et al., (2019) established the recent evolution of an incising stream transporting increasing volumes of gravelly sediment across the Dead Sea shelf, emerging as a result of the lake-level fall. Then, these coarse sediments are transported from the channel mouth and are sorted alongshore at the nearshore environment under seasonal, storm-wave climates, sorting well the coarse gravel comprising the coastal landforms (Eyal et al., 2021). However, the spatiotemporal interactions between the stream and coast and the linkage to or the control of the regional and synoptic-scale hydroclimatology need elaboration to determine the chain of processes. (iii) Its sedimentary fill is well-preserved and accumulated in a terminal basin, thus it is extensively used to reconstruct recent and past sequences, limnogeology, earthquakes, and regional paleoclimatology-paleohydrology (e.g., Bookman et al., 2004; Bartov et al. 2002, 2006; Torfstein et al., 2015, 2013; Huntington, 1911; Neugebauer et al., 2016; Kiro et al., 2017; Palchan et al., 2017; Ahlborn et al., 2018; Ben Dor et al., 2018). However, such studies are mainly interpreted based on specific selected proxies and field associations. The geomorphic causative processes leading to deposition and their respective links to hydroclimatology remain vague.

Therefore, we study here present-day climatic controls on coarse fluvial and coastal sediment transport by means of rain, floods, wind, and waves data from the Dead Sea region. We explore interactions between streams, the coast and the actively forming coarse-clastic sedimentary record (Fig. 1). We search for the specific hydroclimatic events controlling the formation of modern geomorphic/sedimentological record and for potential insights when interpreting similar past deposits. We use a five-years-long (2018-2022) dataset comprised of (i) high-resolution synoptic-scale circulation conditions, (ii) continuous, wind-wave, and rain-floods records, and (iii) storm-scale fluvial and coastal sediment transport measurements by ‘smart’ and marked boulders varying in mass. The manuscript deals with the following questions:

(1) What are the characteristics of atmospheric CPs during which the fluvial and coastal conveyors are activated?

(2) What are the hydroclimatic thresholds for transport and deposition of coarse gravel in this currently regressive lake? Specifically, we focus on intensity-duration of the rainfall, winds, and waves, and the magnitude of the floods.

(3) How do rain-producing floods and wind-driven waves interact to generate a coastal geomorphic record with a specific sedimentary architecture?

(4) What can we learn on past geomorphic records from a modern sedimentary environment generated by the two sedimentary conveyors?

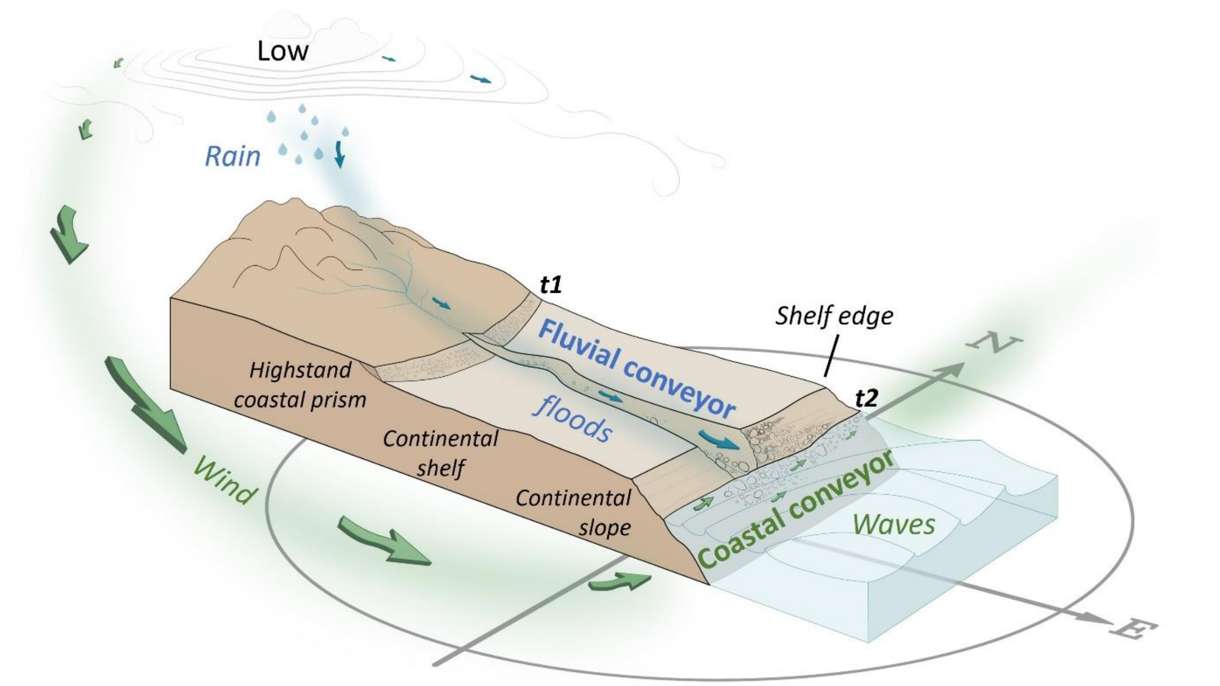

Figure 1: Schematic illustration of the concepts of sediment transport via the stream and coast explored in this study. The forcing/initiation is at the largest scale; low-pressure atmospheric circulation pattern activates both the fluvial sediment conveyor by generating rainstorms and floods that transport coarse sediments into a receding basin (blue), and the coastal sediment conveyor, in which wind-driven waves obliquely attack the beach and generate longshore sediment drift (green). We discuss the dynamic case during water level lowering. t1 and t2 denote the position of highstand and lowstand shorelines. In the case of the Dead Sea t1 represents the middle of the 20th century and t2 the 21st century.

2. The Dead Sea Regional settings

The Dead Sea basin (Fig. 2a) is an actively subsiding tectonic basin along the Dead Sea transform forming a south-north, 150-km long and 15–20 km wide narrow depression (Garfunkel and Ben-Avraham, 1996). Since the late Miocene, the basin is occupied by lakes, expanding and contracting due to climatically-induced water balance and the physiography of the basin (e.g., Zak, 1967; Neev and Emery, 1967; Bartov et al., 2002; Manspeizer, 1985). Respectively, during wet and dry climates, the lake levels rose and fell, and its area extended and contracted (e.g., Bartov et al., 2003, 2006; Bookman et al., 2004; 2006; Enzel et al., 2003). The fluvial and coastal geomorphic responses to these fluctuating lake levels have left well-preserved fan-deltas, paleo-shorelines, and mudflats, related to the Late Pleistocene Lake Lisan (Bowman, 1971; Amit and Gerson, 1986; Frostick and Reid, 1989; Abu Ghazleh and Kempe, 2009) and the Holocene Dead Sea (Enzel et al., 2006., and chapters in Enzel and Bar-Yosef, 2017) (Fig. 2a).

2.1 Geomorphic evolution of streams and coasts in response to shelf and slope exposure

The anthropogenically induced level decline of the modern Dead Sea, at >1 m y^{-1} (Lensky et al., 2005), due to water diversions, results in exposure of landscapes considered as fast-forming analogs to the eustatic emergence of continental shelves and slopes (Dente et al., 2017, 2018; Eyal et al., 2019). The Dead Sea shelf and slope are mainly comprised of laminated, clay silt, lacustrine deposits over which streams (e.g., Dente et al., 2017, 2018, 2021; Ben-Moshe et al., 2008; Bowman et al., 2010; Eyal et al., 2019) and coasts (e.g., Bowman et al., 2000; Bookman et al., 2006; Eyal et al., 2021; Enzel et al., 2022) rapidly evolve and studied at the field scale in real-time and at the storm- to multi-year resolutions. At the northwestern edge of the lake, at the lower reach of the well-studied ephemeral stream of Nahal (wadi) Og (Fig. 2b-d), hydrological connection with the fast-receding coastline is maintained by a cross-shelf incision and elongation. Channel bed steepens (channel slope >1.1%), narrows, and thus increased volumes and clast sizes of coarse sediment are transported to the receding shoreline with time (Eyal et al., 2019). Gravels are comprised of carbonates and some chert and their intermediate axes length range between 0.05-0.4 m. From the tributary mouth, the unsorted bright-color, fluvially-derived sediments are transported northward, sorted along the shore under winter storm waves, and are deposited on top of the dark-brown laminated lacustrine deposits of the newly exposed lake bed (Figs. 1, 2d). This color distinction between the coarse fluvial-coastal and fine lacustrine sediments, along with (i) interplay between fluvial sediment supply and subsequent longshore transport during winter, and (ii) considerable lake-level decline during summer, resulting in an annual separation between individual beach berms, which are practically 'fossilized' at a certain elevation. Through correlation with the well-established lake-level curve, these beach berms are dated to a specific year based on their elevation (Ben Moshe et al., 2008; Eyal et al., 2019; Enzel et al., 2022). The volume of sediment stored in each of these well-preserved beach berms is approximated to a triangular pyramid geometry (Eyal et al., 2019). This volume is attributed solely to the fluvially-derived sediments as there is no additional coarse sediment contribution from the updrift direction (south) or from nearby gullies draining local muddy areas of the shelf. The longshore transport and sorting were measured, quantified, and modelled at the individual storm scale, and it was concluded to be a direct manifestation of wave climate (Eyal et al., 2021).

2.2 Hydroclimate

2.2.1 The potential synoptic-scale climatic drivers at the eastern Mediterranean

Four major synoptic systems prevail in the eastern Mediterranean during wind and rain storms that affect the Dead Sea region:

(i) In winter (mainly December-February), Mediterranean cyclones (MCs) (e.g., Alpert et al., 1990a), also termed Syrian or Cyprus lows, depending on the respective location of their centers, dominate the stormy weather (Alpert et al., 1990a; Alpert and Shay-El, 1994). These extratropical cyclones draw moisture from the Mediterranean and convert it into moderate-intensity rainfall over broad areas (e.g., Ziv et al., 2015; Kushnir et al., 2017). At the regional scale, during the passage of these storms, winds are generally changing from easterlies into westerlies.

(ii) In autumn (October-December), Red Sea troughs (RSTs) are most common (e.g., Kahana et al., 2002). While their "active" variant (ARST) generates localized and intense rainfall with high spatial variability (Kahana et al., 2002; Armon et al., 2018, 2019, 2020; Dayan and Morin, 2006; Belachsen et al., 2017; de Vries et al., 2013; Tsvieli and Zangvil, 2007), the non-active RST usually brings dry easterly winds at the surface (Saaroni et al., 1998).

(iii) In spring (March-May), Sharav lows are frequent in the southeastern Mediterranean (Northern Egypt and Israel), generating warm and dusty winds (e.g., Alpert and Ziv, 1989) with rarely occurring rains and high-velocity westerly winds following their passage over the area.

(iv) In summer (June-September), the Persian trough (PT) prevails; low pressure trough extending from the Persian Gulf to the northeast, along with a subtropical high that borders it from the southwest (Alpert et al., 1990b); rainfall is scarce as large-scale atmospheric subsidence dominates the region (Rodwell and Hoskins, 1996; Goldreich, 2003; Kushnir et al., 2017; Tyrlis and Lelieveld, 2013; Lensky and Dayan, 2015), and winds are rather consistently flowing from the north-west (e.g., Tyrlis and Lelieveld, 2013; Dayan et al., 2017).

2.2.2 The fluvial sediment conveyor

Most of the precipitation that produces flash-floods in the Dead Sea region occurs in the heart of the winter, between November to March, while the full wet season lasts from October to May (Fig. 3a). Annually, the region experiences approximately 20 MCs during winter and early spring with rainstorms typically lasting 2–3 days (Alpert et al., 2004a; Saaroni et al., 2010) generating relatively high-volume floods (Enzel et al., 2003, 2008; Kushnir et al., 2017; Armon et al., 2018; Shentsis et al., 2012). Smaller number of rainstorms during the autumn and spring are associated with ARSTs (Kahana et al., 2002; Armon et al., 2018).

The western water divide of the larger Dead Sea tributaries is at the Judean Mountains with peaks up to ~1000 meters above sea level (masl) and Mediterranean/semi-arid climate (Fig. 2b). From the water divide eastwards, the topography steeply slopes down to the Dead Sea at elevation of ~437 meters (in 2022) below sea level (mbsl) over a short distance of ~30 km, resulting in a sharp climatic gradient (Fig. 3a) due to the orographic rain-shadow effect (Goldreich, 2003; Kushnir et al., 2017). Thus, streams draining into the Dead Sea from the west are ephemeral and are subjected to flash-floods during sufficient storm rainfall (e.g., Morin et al., 2009). For example, in the Nahal Og watershed (137 km^2), the climatic gradient ranges from >500 mm y^{-1} in the western headwaters to as low as ~50 mm y^{-1} at the Dead Sea shore (Figs. 2b, 3a). The mean annual total rain volume falling over the basin is ~$40x10^6$ m^{3}y^{-1} (Haviv, 2007; Ben Moshe et al., 2008), of which only a small fraction reaches the lake. The highest peak discharge estimated for the stream by high-water marks after the rare flood of 2006, is 330 m^3 s^{-1} (Arbel et al., 2009). In Eyal et al. (2019), direct observations of flow marks at a specific location along the channel were interpreted to represent the peak discharge of the common floods of ~20 m^3 s^{-1}. Floods, lasting from a few hours and up to a day, are generally short and respond quickly to high-intensity rain (e.g., Morin et al., 2009).

2.2.3 The coastal sediment conveyor

Winds along the Dead Sea have a bimodal directional distribution of either northerly or southerly direction (Fig. 3b,c) affected by the steep orography and north-south elongation of the Dead Sea rift (Bitan, 1974, 1976; Segal et al., 1983; Vüllers et al., 2018; Kunin et al., 2019). During summer, the diurnal cycle dominates with dry and warm northerly winds (<10 m s^{-1}) blowing stronger at night-time and weaker during the day, attributed to the meso-scale circulation of the Mediterranean Sea breeze (Alpert et al., 1997; Gertman and Hecht, 2002; Lensky and Dayan, 2012; Lensky et al., 2018; Hamdani et al., 2018; Kunin et al., 2019; Naor et al., 2017). During winter, the diurnal cycle is less dominant as the abovementioned synoptic scale circulation governs (Hamdani et al., 2018) with southern windstorms, <20 m s^{-1}, lasting from a few hours to three days, blowing over the ∼40 km south-to-north lake fetch (Eyal et al., 2021). These high-magnitude winter windstorms generate steep waves with a maximum height of ∼4 m, periods of ∼4 s, and wavelengths of ∼25 m along the northeastern shores of the Dead

Sea (Eyal et al., 2021); the high viscosity\density of the brine (Weisbrod et al., 2016) may explain the steepness of the observed wave. During storms, waves approach the coast at ~45° (Eyal et al., 2021), forming optimal conditions for unidirectional longshore drift (Longuet-Higgins, 1970; Van Hijum and Pilarczyk, 1982; Ashton and Giosan, 2011). Along the waterline of the Nahal Og coast, fluvially-derived gravels are distributed over a 20–30 m wide strip, covering the lake floor by a monolayer, extending to a water depth of ~2.5 m; at this depth, transitions to sandy-silty wave ripples are documented. The longshore transport and sorting of the coarse gravel and their link to the wave climate were presented in Eyal et al., (2021) for three intensively monitored storms.

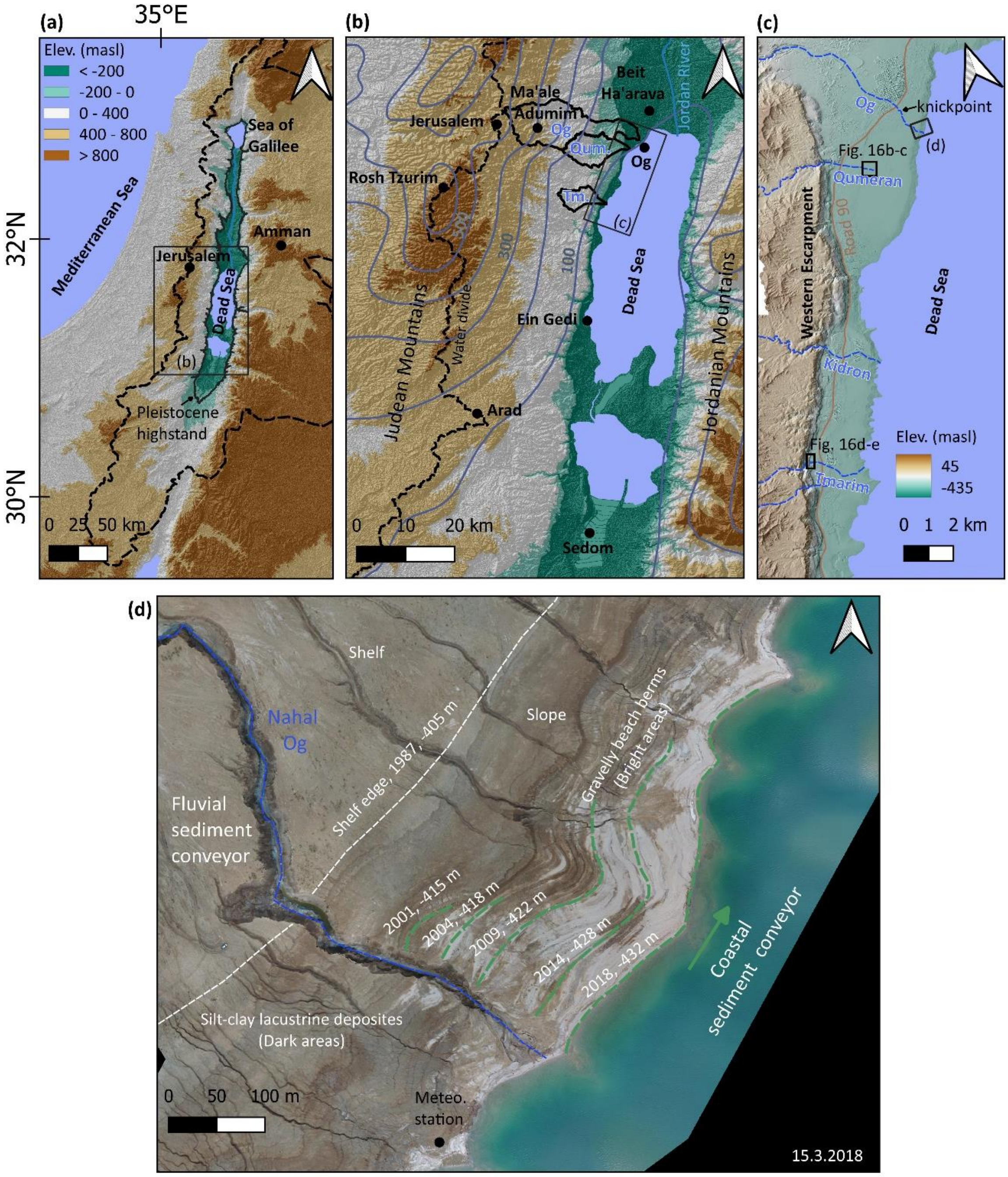

Figure 2: Regional setting. (a) The eastern Mediterranean; shown are the Dead Sea watershed (black dashed line) and the highstand of the Late Pleistocene Lake Lisan, the predecessor of the Dead Sea (black line). (b) The Dead Sea region. Shown are the regional water divide of the Judean Mountains (dashed black line) and the watersheds of the studied tributaries: Og (Og), Qumeran (Qum.) and Tmarim (Tm.) (black polygons). Grey contours are isohyets (mean annual precipitation in mm y^{-1}). They present the rain shadow of the Judean Mountains towards the Dead Sea valley. Black dots are meteorological stations used in this study. (c) The tributaries draining into the north-western Dead Sea (blue dashed lines) and the Dead Sea western escarpment. (d) Aerial photograph of the lower reach of Nahal Og emphasizing the fluvial and coastal conveyors; note the increasing extension farther north, from the stream mouth, of the coastal gravel with lowering of the lake (green lines). It should be stressed that the tributaries north of Nahal Og drain the mudflat and do not carry gravel. Modified from Eyal et al., 2021. We adopt for the Dead Sea margins the global terminology of shelf and slope because of their similar geometry (see Eyal et al., 2019).

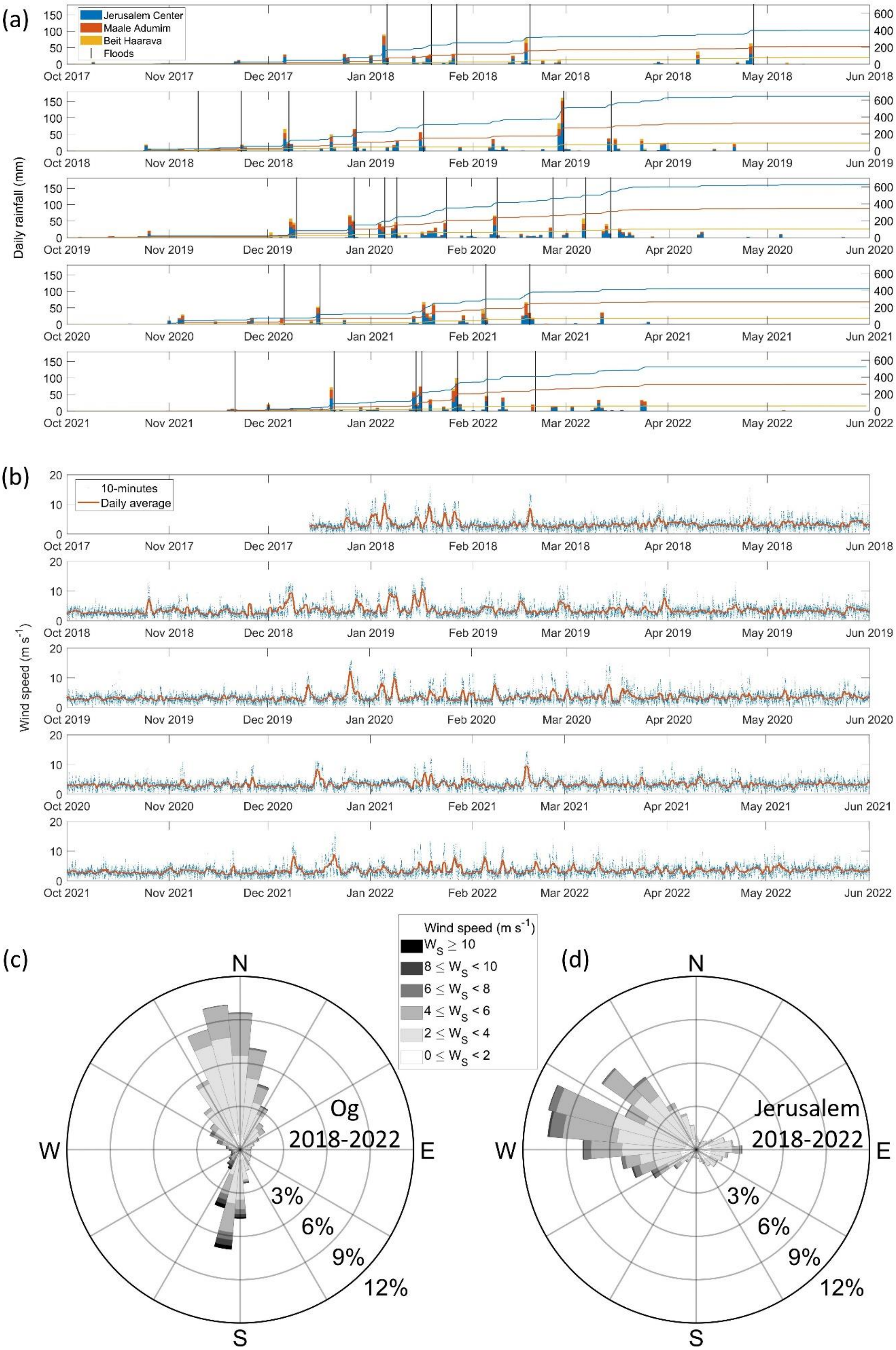
(a)
Jerusalem Center
Maale Adumim
Beit Haarava
Floods
Daily rainfall (mm)
Seasonal rainfall (mm)
Oct 2017
Nov 2017
Dec 2017
Jan 2018
Feb 2018
Mar 2018
Apr 2018
May 2018
Jun 2018
(b)
10-minutes
Daily average
Wind speed (m s^{-1})
(c)
(d)
Wind speed (m s^{-1})
$W_S \geq 10$
$8 \leq W_S < 10$
$6 \leq W_S < 8$
$4 \leq W_S < 6$
$2 \leq W_S < 4$
$0 \leq W_S < 2$
N
E
S
W
Og
2018-2022
Jerusalem
2018-2022
3%
6%
9%
12%

Figure 3: Rainfall and wind forcing during the five, intensively measured hydrological years: December 2017- June 2022. (a) Daily (bars, left-axis) and seasonal cumulative (lines; right-axis) rainfall measured, from west to east, in Jerusalem (blue), Ma'ale Adumim (orange), and Beit-HaArava (yellow), representing the headwaters, the center, and lower areas of the watershed, respectively (stations locations are presented in Fig. 2b). Vertical black lines are occurrences of floods (Table S1 in the supplement). Note that most storms affect the entire region with consistent decline in rainfall amounts away from the water divide. (b) 10-minutes (blue crosses) and daily average (orange line) wind speed at Nahal Og mouth. Windrose for (c) Nahal Og (-430 masl) and (d) Jerusalem (835 masl) representing the frequency and directionality of winds during the study period. Note the orthogonal wind directions; in the upper watershed it is dominated by westerlies, while at the same time, within the Dead Sea rift valley, it is dominated by northerlies and southerlies.

3. Methods, data, and analyses

We assembled a high-resolution, rich dataset to unfold the chain of processes from CPs to the coarse-gravelly sediments along the coasts of the Dead Sea. The dataset is comprised of: (1) Five-year long, continuous monitoring of winds, waves, lake level, rain and flood hydrology. (2) Storm-scale sediment transport documented in the channel and shore. (3) A combination of this dataset with atmospheric CPs using atmospheric reanalysis. These observations constitute a one-of-a-kind dataset of coeval processes at such a resolution, undoubtedly for this region and probably for elsewhere. Additionally, although these observations are based on only five years of data, a comparison of the rainfall and wind timeseries with records of adjacent long-term weather stations, indicates that these five years well represent the mean climatic conditions (Sect. S2 in the supplement).

3.1 Field measurements

Wind speed and direction at 10-min intervals were (a) measured at the Nahal Og mouth by a Gill-WindSonic sensor located ~5 m above the lake surface, between December 2017 and June 2022, and (b) obtained from the Israel Meteorological Service for the stations of Jerusalem Center (1999-2022), Ma'ale Adumim (2007-2022), Ein Gedi (2007-2021), Rosh Tzurim (2001-2021), Arad (1999-2021), Sedom (1999-2021) and Beit Ha'arava (2008-2022) (Fig. 2b).

Waves were measured at 4 Hz frequency by a water pressure sensor (Keller-PAA 36 Xi W) at water depth range of 12 (December 2017) to 8 m (June 2022). Significant wave height and period were analyzed, accounting for the attenuation of wave-induced pressure variation with water depth, and the temporal change of water depth due to lake-level decline (Karimpour and Chen, 2017). From the continuous 4 Hz data, differences between maximum and minimum pressure at 10-min resolution were normalized between 0 (no waves) and 1 (highest observed wave height, H = 4 m) and used as proxies for the significant wave height (Fig. S3, Eyal et al., 2021). This was done as the long time-series of 4 Hz measurements is incomplete. This analysis was validated by 16 Hz measurements of RBR-solo-wave pressure sensor, deployed at 5-m water depth during three storm waves.

Rain data at 10-min intervals were obtained from the Israel Meteorological Service for the stations of Jerusalem Center (1999-2022), Ma'ale Adumim (2008-2022) and Beit Ha'arava (2008-2022).

A *Flood Hydrology* data set was gathered from several sources (see Sect. S1 in the supplement), as no direct discharge measurements exist in the watershed: (a) Observations obtained by Time-Lapse Cameras (TLCs) and real-time field surveys, from which hydrographs were estimated using the manning formula (as in Eyal et al.,

2019) (when high flows occurred at night, high water marks were estimated from the daylight video). (b) Flood reports obtained from the Israel Flash-flood Forecasting Center, Water Authority of Israel. (c) Flood reports obtained from the Desert Floods Research Center categorized into no flood, weak flood, moderate flood, and large flood. (d) Social network reports (e.g., Borga et al., 2019), providing an almost complete binary series of yes/no flood occurrences and their estimated magnitude. These observations were synthesized to classify the floods into four categories according to the estimated flood peak-discharge: low-flow floods, which due to transmission losses do not reach the lake, weak floods, moderate floods, and large floods. Estimation of the extremity of the peak discharge for each class was evaluated according to Rinat et al., 2021 (their Fig. 8). Cross-checking between the information sources and close monitoring of the events during the measurement interval of 2017-2022 provides a high level of certainty about the completeness of the flood time series. However, it must be noted that hydrograph estimation gives rough values rather than exact high-resolution measurement data.

The *Dead Sea level* was obtained from Water Authority of Israel at a monthly resolution.

Sediment transport was measured using boulders with masses ranging between 0.5-100 kg. (a) Many (<100) boulders were positioned in the upstream channel to estimate transport distances during a single flood. (b) Eighty painted boulders and five "smart" boulders were positioned along the beach to quantify longshore displacement during individual storm, as described in Eyal et al., 2021.

Late Pleistocene to modern fan-deltas were analyzed by: (a) Airborne LiDAR-based DEMs for 2020, with horizontal and vertical resolutions of 0.5 and 0.25 m pixel^{-1}, respectively (obtained from the Geological Survey of Israel). (b) Orthophoto imagery and georeferenced aerial photographs from the years 1945, 1967, 1980, 1987 (obtained from the Survey of Israel). (c) A satellite image from 1971 (Corona mission, Grosse et al., 2005; data available from https://earthexplorer.usgs.gov) with a spatial resolution of up to several meters per pixel. These images were used to examine landscape change preceding the available LiDAR-based DEMs. They were also used for mapping and determining the altitude of shorelines of the late 20th and 21st centuries, recognized on both air photographs and LiDAR and of Late Pleistocene shorelines in Nahal Tmarim (location in Fig. 2b,c). DEM and hill shade of 30 m pixel^{-1} resolution obtained from Geological Survey of Israel were used for location maps (Figs. 2a,b, and 10a)

3.2 Data analysis

3.2.1 Storm detection

Over 120 storm waves were defined according to a physical threshold of the critical wave height for mobilization of a 1 kg clast: H_{cr}=~0.6 m as determined previously by Eyal et al., 2021. A one-day interval was selected as a separation between individual storms. The timing of storm initiation and cessation was obtained using a lower wave height threshold (e.g., Molina et al., 2019), H=~0.15 m, which is a sufficiently lower value to account for the entire storm-wave duration (Fig. 4). As the waves are wind-driven (see below Sect. 4), windstorms were defined according to the timing of the storm waves. This was done by applying the timing of the wave initiation and cessation to the wind speed timeseries and redefining the windstorm initiation and cessation according to a wind speed daily mean threshold of 3 m s^{-1} (Fig. 4). This threshold optimally represents the storms following a comparison with a range of thresholds (0.5 – 5 m s^{-1}). The storm peak is defined as the maximal wind value in the interval between the windstorm initiation and cessation. Rainfall was analyzed at hourly intervals, accumulated from the 10 minutes data. Thirty-two flood-producing rainstorms were defined by detecting rainstorm peaks using a one-day time interval before and after flood initiation. The timing of rainstorm initiation and cessation were redefined using a 0.1 mm h^{-1} threshold and a separation of at least six hours between successive storms (e.g., Marra et al., 2020).

3.2.2 Synoptic classification

We classified wind-waves-rain storms into four classes representing the most common synoptic circulation patterns prevailing in the region (Sect. 2.2.1): Mediterranean Cyclones (MCs), Active Red Sea Troughs (ARSTs), Persian Troughs (PTs), and Sharav Lows (SLs). To do so, we generalized the 19 classes obtained by the semi-objective synoptic classification introduced by Alpert et al. (2004b) for the eastern Mediterranean, which is based on daily (12:00 UTC) meteorological fields at the 1000 hPa pressure level from the NCEP/NCAR reanalysis (2.5^0 spatial resolution). We classified a storm as a MC if one of the storm days was considered as a MC. ARST was defined if one of the storm days was considered as ARST with no MC prevalence. SL was classified if one of the days during the storm was classified as SL, regardless of the other classes obtained by the semi-objective classification. PT was classified only if it appeared in the summer months between June and September (e.g., Ziv et al., 2004), even if it appeared with other classes. Otherwise, the semi-objective PT was classified as a MC in accordance with weak cyclones manifested as a shallow trough in the northeastern Mediterranean (Ziv et al., 2022). Given that the final stage of MCs is usually characterized by the dissipation of the low and increased dominance of a high (e.g., Armon et al., 2019), we decided to manually inspect 13 cases in which the semi-objective classification yielded a high. Similar to Marra et al., (2021), we realized that these cases were actually the final stages of MCs.

3.2.3 Composite and individual storm CPs

Composite and individual storm CPs were analyzed using data from the European Center of Medium-range Weather Forecasts (ECMWF) Reanalysis model 5 (ERA5; Hersbach et al., 2020). Sea level pressure and 10-m above ground wind maps were produced for the wind-wave storms at their onset, peak and cessation at a resolution of 0.5° per pixel. Composite maps were obtained for (i) the mean conditions during the different storm parts both for all CPs grouped together and separately for, (ii) the lowest, intermediate, and highest terciles of the wave energy, duration, and wave height, and (iii) the climatology of wave-producing CPs, non-wave-producing CPs, and the anomaly of the wave-producing CP compared to the mean conditions of CP for the same period (2017-2022).

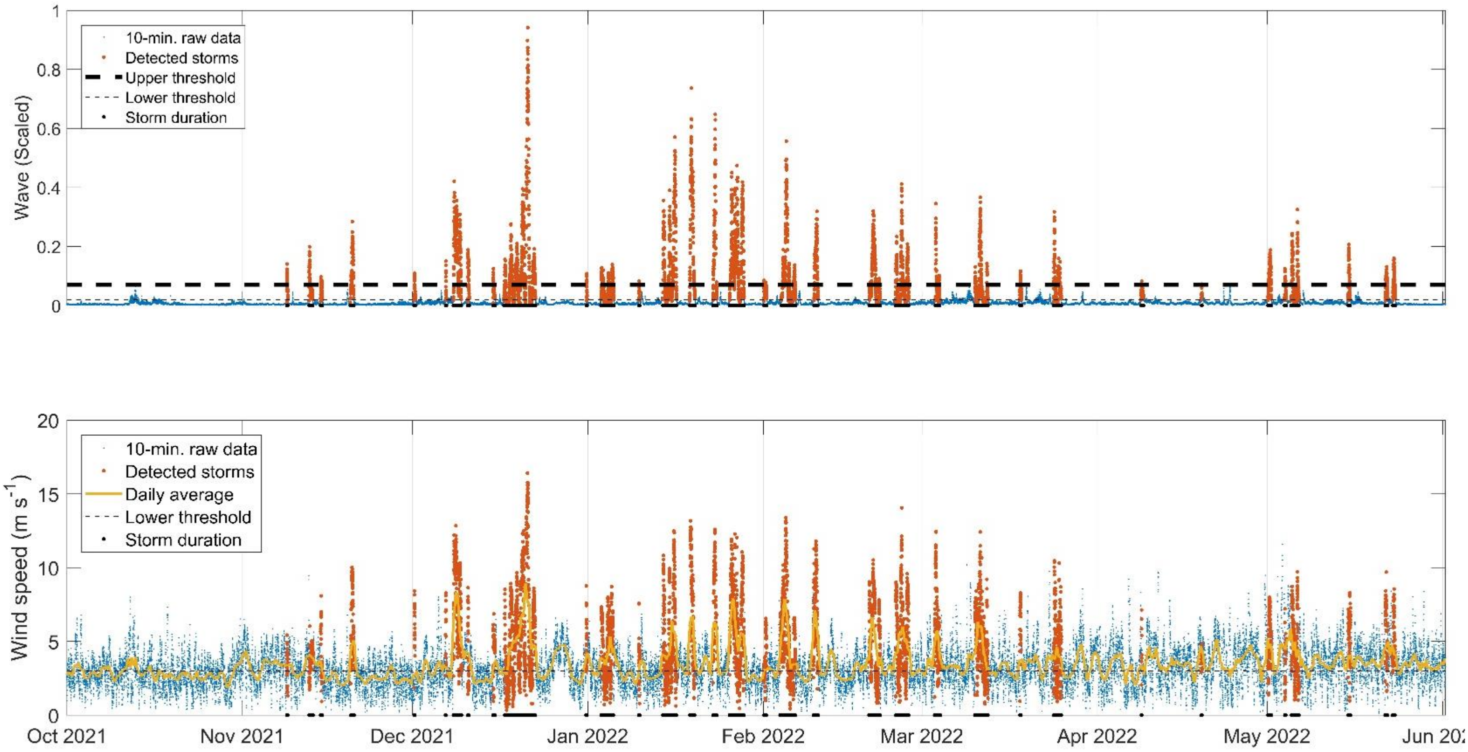

337

338 **Figure 4: An example of wind-wave storm detection during one hydrological year (2021-2022). (a) Storm waves (orange**
339 **dots) were detected by an upper physical threshold following Eyal et al., 2021 (thick dashed black line), with the full**
340 **duration (black dots marked on the x-axis) defined by a lower threshold (thin dashed black line). (b) Windstorms**
341 **(orange dots) were defined according to the detected storm waves, with the full duration defined by a lower threshold**
342 **(dashed black line) following the daily average of the wind speed (yellow line).**

4. The fluvial and coastal sediment conveyors and their synoptic-scale hydroclimatic control

We present insights from five representative storm-scale case studies in Sect. 4.1 for which we have detailed measurements of sediment transport in the stream and coast under the forcing of atmospheric CPs, winds and waves, rain, and floods (Figs. 5-9). Each component is described with respect to the timeline of a wind-wave storm from its onset, rise, peak, decay, and cessation. Then, in Sect. 4.2, we present the separation of the wind field into two levels with perpendicular directions, i.e., the regional surface wind during storms both outside and inside the Dead Sea rift valley (Fig. 10). In Sect. 4.3 we generalize the processes leading to the activation of the two sediment conveyors with a full analysis of the wind-wave storms and floods of the past five years with their synoptic- and meso-scale climatology (Figs. 11-13). Given that MCs stand out as the main activators of the sediment conveyors (Sect. 4.3 and Fig. 11), we describe the results according to the evolution of this synoptic-scale CP and add information on other CPs when necessary.

4.1 The stream and coast at the storm scale

4.1.1 Storm-scale atmospheric CPs

At the onset of the wind-wave storms, the centers of the MCs are located north of the study region: (i) In the vicinity of Greece, as far as ~1500 km northwest of the Dead Sea (Fig. 5c). (ii) In the eastern Mediterranean near Cyprus, ~500 km northwest of the Dead Sea (Figs. 6-7c). (iii) In Syria or Iraq, 500-700 km north-northeast of the Dead Sea (Fig. 8c). Only seldom storms occur when the cyclone is nearer to the Dead Sea, in southern Israel (Fig. 9, see a more detailed description of such a storm in Dayan et al., (2021) and in Rinat et al., (2021). The prevailing storm circulation is of anti-clockwise westerly/south-westerly winds. Towards the storm peak, MCs focus, i.e., become smaller, deepen, and move eastwards (Figs. 5-8d). In mature and ending stages of impacting MCs, the regional westerly flow and lowered inversion (Armon et al., 2019; Goldreich et al., 2004) are manifested by 'mountain waves'; i.e., south-north elongated cloudy crests extending over the Jordanian mountains and plateau (Fig. 6h). The storm is over when the low-pressure systems become larger, shallower, move further to the east, and a high-pressure system invades the region (Figs. 5-8e).

4.1.2 Local wind and waves

While at the regional scale westerly flows dominates, at the local scale, over the Dead Sea itself, a sharp rise of pronounced southern winds characterizes the onset of storms under MCs as measured along the Dead Sea shores (Figs. 5-9b). With the intensification of the winds to >10 m s^{-1} and up to 20 m s^{-1}, northward-propagating waves also intensify (Fig. 5-9b). At the end of the storm, diverse directionality that characterizes the pre- and post-storm intervals of the wind (Figs. 5-9b) prevails, and the wind and waves quickly calm down.

4.1.3 Rain and floods

Rainfall in the drainage basin (Ma'ale Adumim station, Fig. 2b) initiates coevally with the wind-wave storms, normally with intensified rain after or even during the timing of the storm wave peak (Figs. 5, 6a, 7–9a), reaching moderate to high rainfall intensities relative to this dry climate, of > 5 mm h^{-1} for the duration of at least one hour (Figs. 5–9a). Rainfall intensity may comprise of several maxima, and accordingly, the flash-flood hydrograph presents several peaks (Figs. 5, 7, 8a). Flood discharge maxima range between weak (~5 m^3s^{-1}) (Fig. 5a) and the largest flood documented between 2017-2022, with an estimated peak discharge of 120±30 $m^3 s^{-1}$ (Fig. 8a). These floods typically last <24 h lagging a few hours after the rain peak; this important observation indicates that sediments are delivered to the stream mouth towards the decay or end of the respective windstorm or storm wave.

4.1.4 Sediment transport

With the rise of winds and waves and exceedance of the critical wave height (Fig. 4), certain clasts are mobilized according to their mass as indicated by the recorded, during-storm accelerations and rotations of individual clasts (Fig. 6f, Eyal et al., 2021). During the storm peak, the highest accelerations and rotations are recorded (Fig. 6f). By the end of the storm wave, field observations and measurements indicate that the gravels are sorted along the shore as the displacement decrease with increasing clast mass, according to a power law (Eyal et al., 2021) (Figs. 5f, 6g, 9f). During individual storms, larger clasts weighing ten of kilograms are transported to tens of meters, and finer clasts weighing kilograms are transported hundreds of meters along the shore (Figs. 5f, 6g, 9f). Coevally, or by the end of the storm waves, a flood reaches the stream outlet into the Dead Sea (Figs. 5–9a) transporting at a single, relatively low-discharge flood, cobble-boulder sized clasts, up to >10 kg each, along the channel incised across the one-kilometer-wide muddy shelf (Fig. 5a). The transport rate of boulders per single event along the shore is one to two orders of magnitudes smaller relative to the transport in the stream. In the common case of floods that are generated after the storm wave, delta deposition and sediment progradation of up to 20 m offshore were observed at the channel mouth (Fig. 9g-i). In such a case, the storm-scale activity of the coastal conveyor precedes the fluvial conveyor, and longshore transport and sorting of the fluvio-deltaic sediments can only happen during the next storm. A different case occurs when floods practically do not reach the lake and only the coast is activated by the storm, reworking the sediments delivered by the previous storms in the season (Fig. 6a).

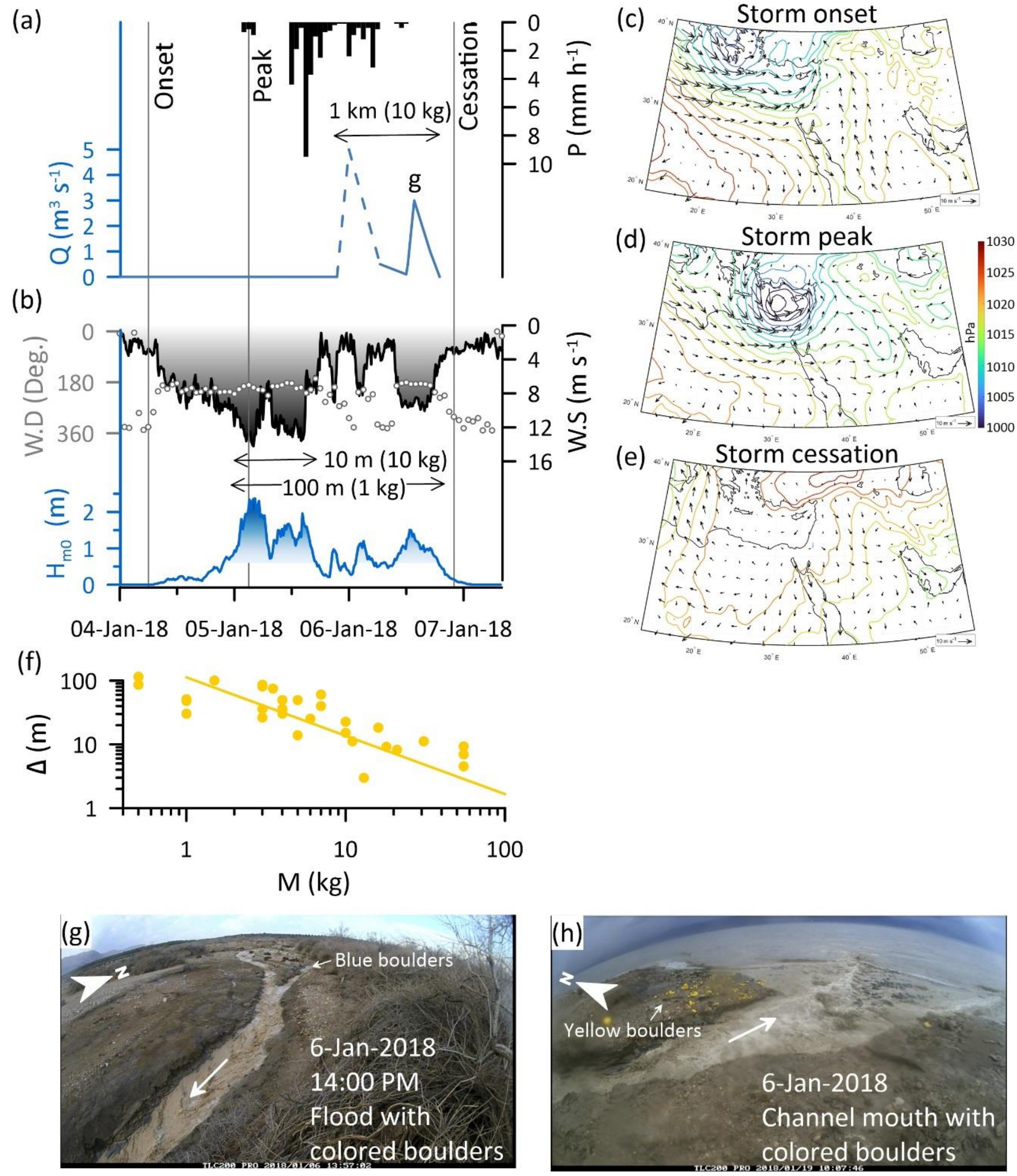

Figure 5: Storm-scale observations (4-7 January, 2018) of the chain of processes from the synoptic scale atmospheric circulation that generate rainstorms-producing floods, wind-wave storms, resulting in fluvial and coastal sediment transport. (a) Hourly rainfall (P, Ma'ale Adumim, Fig. 2b), flood discharge (Q, solid line based on TLC and dashed line based on high-water marks). During this flood, colored cobbles-boulders were transported across the entire 1 km shelf width into the Dead Sea. (b) Wind (W.S-wind speed, black gradient fill darkens towards higher wind speed, W.D-wind direction in dots) and wave height (H-significant wave height, blue gradient fill indicates waves above transport threshold, darkens towards higher waves). (c, d, and e) CP maps of a deep Mediterranean Cyclone plotted according to the onset, peak, and cessation of wind, respectively. (f) Longshore displacement (Δ) of various-mass boulders (M) (yellow dots), transported from the channel mouth northward and sorted alongshore according to a power-law (yellow line), following Eyal et al., 2021. (g) The flood at the stream knickpoint where boulders were colored. (h) The flood flows into the Dead Sea, where coastal boulders are colored.

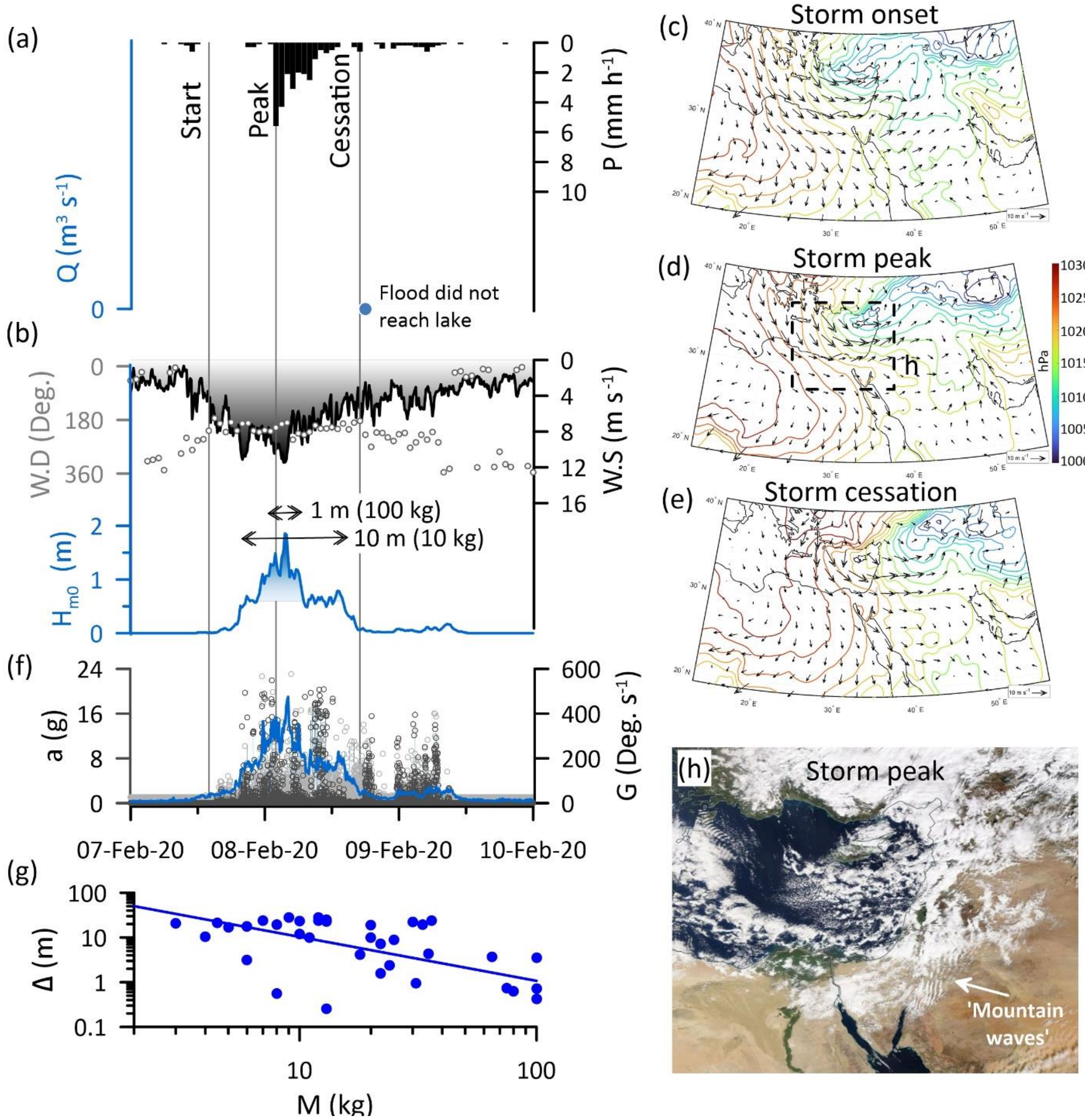

Figure 6: Storm-scale observations (7-9 February, 2020) of the chain of processes from the synoptic- scale atmospheric circulation that generate rainstorms-producing floods, wind-wave storms, resulting in fluvial and coastal sediment transport. (a) Hourly rainfall (P, Ma'ale Adumim, Fig. 2b), flood was generated but did not reach the lake. The timing of a first wave is marked by a blue dot. (b) Wind (W.S-wind speed, black gradient darkens towards higher wind speed, W.D-wind direction in dots), and wave height (H-significant wave height, blue gradient fill indicates waves above transport threshold, darkens towards higher waves). (c, d, and e) CP maps of a Mediterranean Cyclone plotted according to the onset, peak, and cessation of wind, respectively. (f) Resultant acceleration (a, grey dots) and rotations (G, black dots) recorded by five, various-mass smart boulders indicating the real-time motions of clasts under storm waves, following Eyal et al., 2021. (g) Longshore displacement (Δ) of various-mass boulders (M) (blue dots), transported from the channel mouth northward and sorted alongshore according to a power-law (blue line). (h) Aerial photograph of the eastern Mediterranean during the storm peak (8 February 2020) obtained from https://worldview.earthdata.nasa.gov/, location in (d). Note the south-north elongated cloudy crests termed 'mountain waves', indicating on the synoptic westerly air flow.

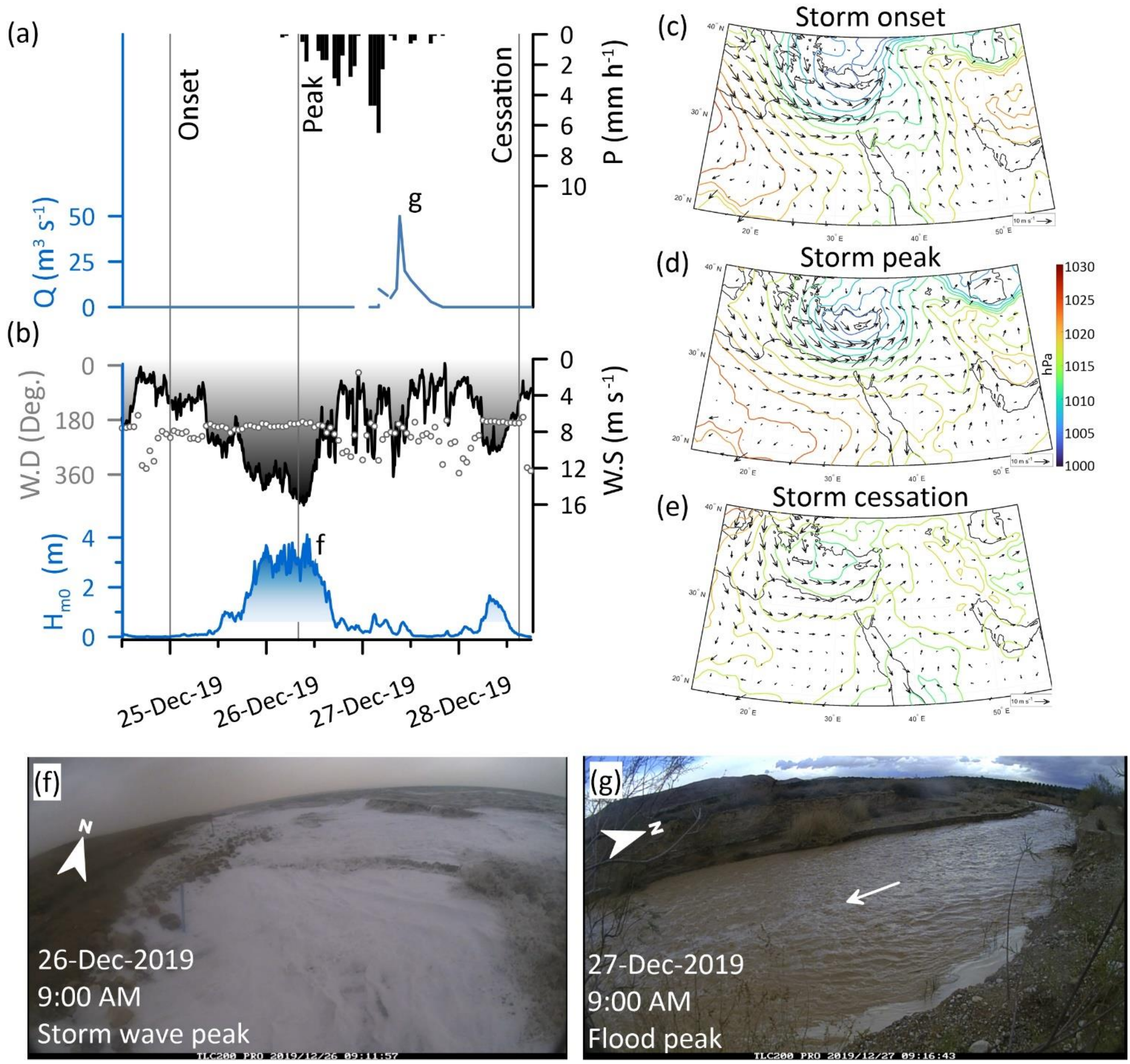

Figure 7: Storm-scale observations (25-28 December, 2019) of the chain of processes from the synoptic-scale atmospheric circulation that generate rainstorms-producing floods, wind-wave storms, resulting in fluvial and coastal sediment transport. (a) Hourly rainfall (P, Ma'ale Adumim, Fig. 2b), flood discharge (Q, solid line-TLC). Wind (W.S-wind speed, black gradient darkens towards higher wind speed, W.D-wind direction in dots) and wave height (H-significant wave height, blue gradient fill indicates waves above transport threshold, darkens towards higher waves). This storm wave was the largest documented in our record (Video supplement). (c, d, and e) CP maps of a deep Mediterranean Cyclone plotted according to the onset, peak, and cessation of wind, respectively. (f) The storm wave during its peak, which is the highest in our record. (g) The flood peak downstream to road 90 (location in Fig. 2c).

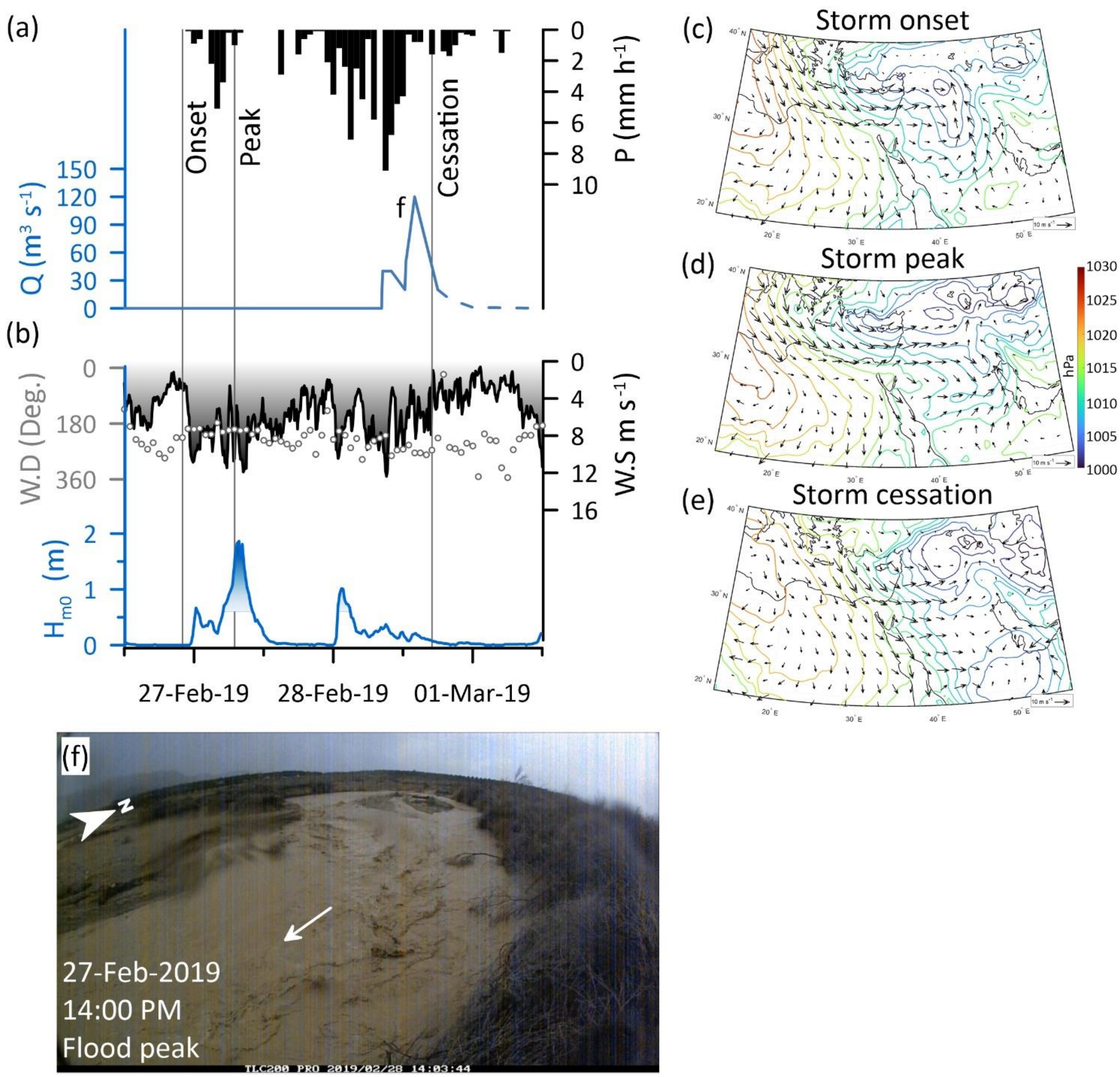

Figure 8: Storm-scale observations (27-28, February 2019) of the chain of processes from the synoptic scale atmospheric circulation that generate rainstorms-producing floods, wind-wave storms, resulting in fluvial and coastal sediment transport. (a) Hourly rainfall (P, Ma'ale Adumim, Fig. 2b), flood discharge (Q, solid line-TLC). This flood was the largest documented in our record (Video supplement). (b) Wind (W.S-wind speed, black gradient darkens towards higher wind speed, W.D-wind direction in dots) and wave height (H-significant wave height, blue gradient fill indicates waves above transport threshold, darkens towards higher waves). (c, d, and e) CP maps of a Mediterranean Cyclone centered to the east of the Mediterranean, with an extended trough to the eastern Mediterranean, plotted according to the onset, peak, and cessation of wind, respectively. (f) The flood peak downstream of Highway 90 (location in Fig. 2c).

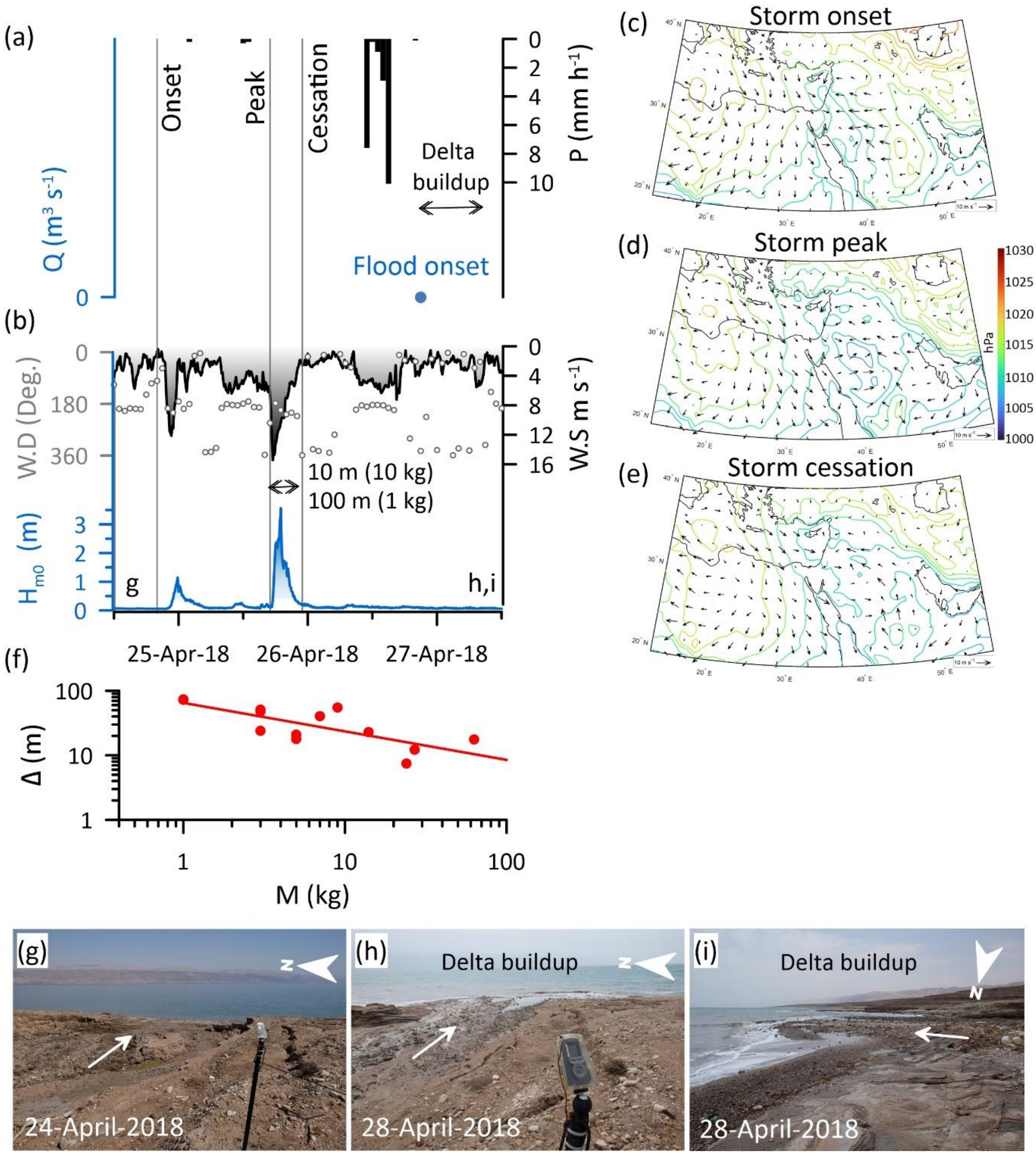

Figure 9: Storm-scale observations (25-27 April, 2018) of the chain of processes from the synoptic-scale atmospheric circulation that generate rainstorms-producing floods, wind-wave storms, resulting in fluvial and coastal sediment transport. (a) Hourly rainfall (P, Ma'ale Adumim, Fig. 2b). The flood discharge was high, as indicated from a field visit during this storm. (b) Wind (W.S-wind speed, black gradient darkens towards higher wind speed, W.D-wind direction in dots) and wave height (H-significant wave height, blue gradient fill indicates waves above transport threshold, darkens towards higher waves). (c, d, and e) CP maps of a southern-centered Mediterranean Cyclone plotted according to the onset, peak, and cessation of wind, respectively. This storm also was discussed in detail in Rinat et al., (2021) and Dayan et al., (2021). (f) Longshore displacement (Δ) of various-mass boulders (M) (red dots), transported from the channel mouth northward and sorted alongshore according to a power-law (red line), following Eyal et al., 2021. (g) The channel mouth before the storm. (h and i) The channel mouth after the flood ends with prominent fan-delta progradation of ~20 m offshore.

4.2 Synoptic-scale and topographically funnelled surface winds activating the two perpendicular sediment conveyors

During MC storms, synoptic-scale westerly circulation is consistent with measurements of surface wind in ground stations, located along a south-north transect of the 600-1000 masl water divide at the Judean Mountains (Fig. 10a-d). Coevally, a transect of the winds within the Dead Sea rift valley at an elevation of ~400 mbsl, ~30 km east of and sub-parallel to the water divide, indicates that the high-magnitude surface winds have a clear southern directionality (Fig. 10a, e-g). We attribute this directionality change, from the regional westerlies into in-rift valley southerlies during the same individual storm, to the orography-funneling effect by the topography of the Dead Sea valley with its south-to-north oriented rift shoulders (e.g., Bitan, 1976). Consequently, we recognize that the winds associated with the main synoptic-scale circulation pattern (MC) splits into two perpendicular directions; these two hydroclimatic generators activate differently the conveyors of the coarse sediments(Figs. 1, 10, Video supplement): (i) Westerlies at high altitudes convey moisture from the Mediterranean Sea, with rainfall amounts tending to increase when air parcels encounter the orographic barrier of the Judean Mountains and then decrease when reaching the rain shadow area of the Dead Sea rift valley (Sharon and Kutiel, 1986; Goldreich, 1994; Marra et al., 2022). This orographic effect is an important permanent feature over the last millions of years since the rift reached its shape. This orography determines the amount and distribution of rainfall over the western Dead Sea watersheds and, in turn, the characteristics of floods, and with them the storm to seasonal timing of sediment delivery into the basin. The conveyance of moisture continues to the east of the Dead Sea and rainfall amount increases again with the upslope flow over the Jordanian mountains >1000 masl (e.g., Armon et al., 2019); as a result, floods are generated, and sediments are delivered to the Dead Sea from its eastern watersheds later or at the very end of the storms. (ii) At the surface, southerlies blow perpendicular to and coeval with the synoptic-scale mountainous winds. The meso-scale funneling of winds blowing over the lake results in south-to-north waves propagation and thus, at the coast, the redistribution of sediments preferentially northwards from the channel mouths along the Dead Sea shores.

Weaker CPs have different air trajectories, but as long as the synoptic winds have a slight southern component, the topography and shape of the Dead Sea rift margins govern, resulting in southerly-funneled winds. For example, under ARST conditions, the synoptic-scale wind is southeasterly, while the actual surface wind measurements are pure southerlies (Fig. S4).

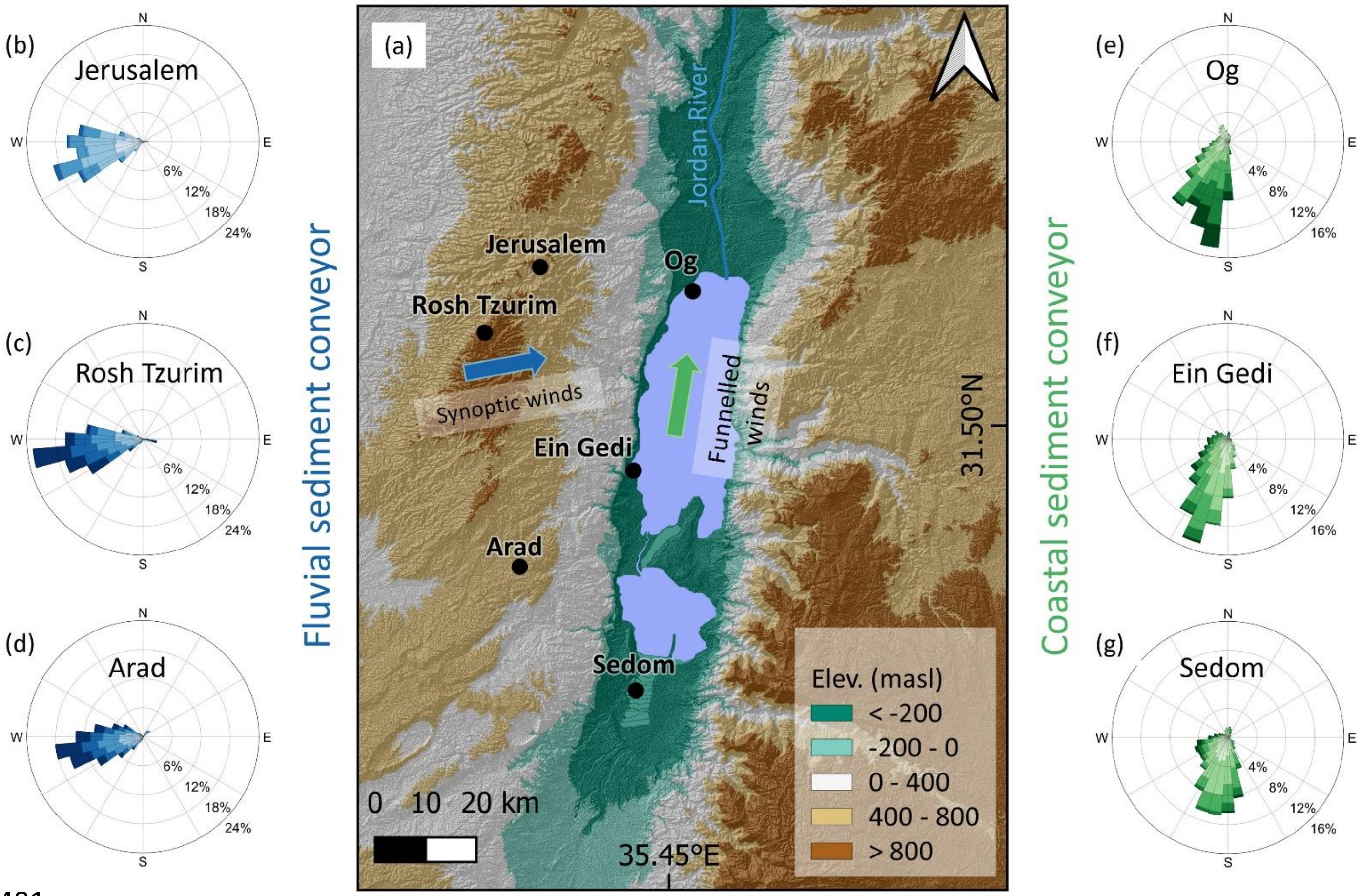

Figure 10: Synoptic and meso-scale windstorms. (a) Location map showing the two perpendicular directions of the winds flow during MC storms. (b, c, and d) Wind roses from three Judean Mountains water divide stations (locations are indicated in the map). These data show the western-southwestern high-magnitude winds during winter storms conveying at high altitudes the moisture for flood generation in the fluvial sediment conveyor (blue coloring). (e, f, and g) Wind roses from inside the Dead Sea rift valley. These data show the change in wind direction as the synoptic scale winds are funneled in the rift and transformed into high-magnitude southerlies that generate the northward propagating storm waves activating the coastal sediment conveyor (green coloring). Legend of the wind roses appear in Fig. 3c-d.

4.3 The sediment conveyors at the seasonal scale under a joint atmospheric circulation generator

4.3.1 The coastal conveyor at the seasonal scale

Like the stream, the coast is activated mainly between December and March (Fig. 11) under MCs located north of the Dead Sea region (Fig. 12). Each of the 128 classified storm waves (i.e., 10–30 storms per winter) are wind driven and are correlated with high magnitude southern winds (Fig. S6). The wind and wave storm durations are very similar or equal (Fig. 12a), ranging between several hours to three days, <1.5 days for the 25-75 percentiles of the wind (Fig. 13a-b). The prevailing CP during 80% of the identified storms is MC (Fig. 12a), also causing the highest storm wave energy with the longest duration of up to 3.5 days (Fig. S5). At the onset of storms, on average, a deep low-pressure system, ~10 hPa below mean, is located in the vicinity of either Cyprus or Syria, exhibited in the composite and anomaly analyses as bi-center lows in these two regions, and the regional wind direction is western, with a slight southern component over southern Israel (Fig. 13d). At storm wave peaks, the area of the low-pressure system contracts and the low moves eastwards (Fig. 13e). Along the Dead Sea, the median wind speed at the storms peak is 10 m s^{-1} with short-term winds of up to ca. 20 m s^{-1} with a clear southern direction. The wind-driven northwards propagating waves, typically lag the regional wind peaks by 0.5-2 h. Median wave height is about ~1 m with maximal height of ~4 m. The cessation of storms is associated with significant shallowing of the MC, appearance of high-pressure system and its advancement from the west, and a change of the mean wind direction into northwesterly winds (Fig. 13f), funneled inside the Dead Sea valley into weaker northerlies.

The non-MC storm waves are generated by low wave-energy CPs, mainly by Active Red Sea Troughs, (15% of storm-waves producing CPs). The other 5% are caused by Persian Troughs and Sharav Lows, generating shorter storms lasting <10 h (Fig. 12a, Fig. S4). Practically, these storms have a minor impact on the coastal geomorphology and sediment transport as the thresholds (as wave height) for the motion of clasts in the coastal conveyor are barely exceeded.

The comparison of the mean climatology of wind-wave producing MCs with the nonproducing MCs, show that wind-wave producing MCs are: (i) characterized by stronger regional westerlies, (ii) ~3 hPa deeper at their center, and (iii) accompanied by an adjacent high of ca. +5 hPa higher pressure, located over Egypt and Turkey. This total difference of ~8 hPa results in steeper pressure gradients from the north and south of the MC and the generation of stronger winds (Fig. 14); these winds are funneled into southerlies at the meso-scale (Fig. 10).

4.3.2 The fluvial conveyor at the seasonal scale

Flood-producing rainstorms in the stream occurred 4-9 times per season. Each of these rainstorms lasted between a few hours and up to two days (Figs. 11, 12b) with a typical duration of 10-15 hours for the 25-75 percentiles (Fig. 13c). These rainstorms have a median peak intensity of 5 mm h^{-1} for the duration of one hour (Fig. 13c), and maximal intensities of up to 20 mm h^{-1} (Fig. 11). Rain depth >10 mm per such a storm generates moderate or larger floods as measured at the center of the Nahal Og watershed (Fig. S7). About 60% of the floods present low discharge (<10 m^3s^{-1}) or attenuate to such low flows that the floods practically do not reach the lake. Moderate floods (9 floods, 28%) experience peak discharge of 10–60 m^3s^{-1} and the high-discharge floods (4 floods, 12%) have an estimated peak discharge of 60–170 m^3s^{-1}. Under rare conditions extreme floods with a peak discharge

>170 m^3s^{-1} can be generated. For example, in 2006, an exceptional discharge of 330 m^3s^{-1} was estimated indirectly in Nahal Og based on high-water marks by Arbel et al. (2009); this is equivalent to a contribution of instantaneous rainfall intensity of 8.7 mm h^{-1} from the entire watershed.

Approximately 85% of the flood-producing rainstorms were generated by MCs, with all the moderate to large floods generated by this circulation pattern (CP). Moreover, these rainstorms occurred coevally with storm waves occurring under the same MCs (Fig. 11). For MCs, rainfall amounts increase with storm duration (Fig. 12b), an observation we attribute to the characteristically continuous, wide coverage of rainfall during MCs (Armon et al., 2018). The finding is coherent with similar analysis that was applied for the adjacent and much larger Lower Jordan River (Armon et al., 2019).

The rest of the flood-producing rainstorms (~15%) are attributed to ARSTs (Fig. 12b). These storms produced low floods during the beginning and end of the hydrological season. This observation emphasizes the control of MCs on geomorphic processes and delivery of sediments to the basin in this region (Fig. 12). For ARSTs, both rainstorm duration and floods occurrence are uncorrelated with rainfall amounts (Fig. 12b); these complex relations are attributed to the short-duration, relatively high-intensity, and localized rainfall associated with ARSTs (e.g., Armon et al., 2018, 2019) that a single rain gauge (Ma’ale Adumim, location in Fig. 2b) cannot capture, biasing the flood-producing rain depth (e.g., Sharon, 1972; Marra and Morin, 2018).

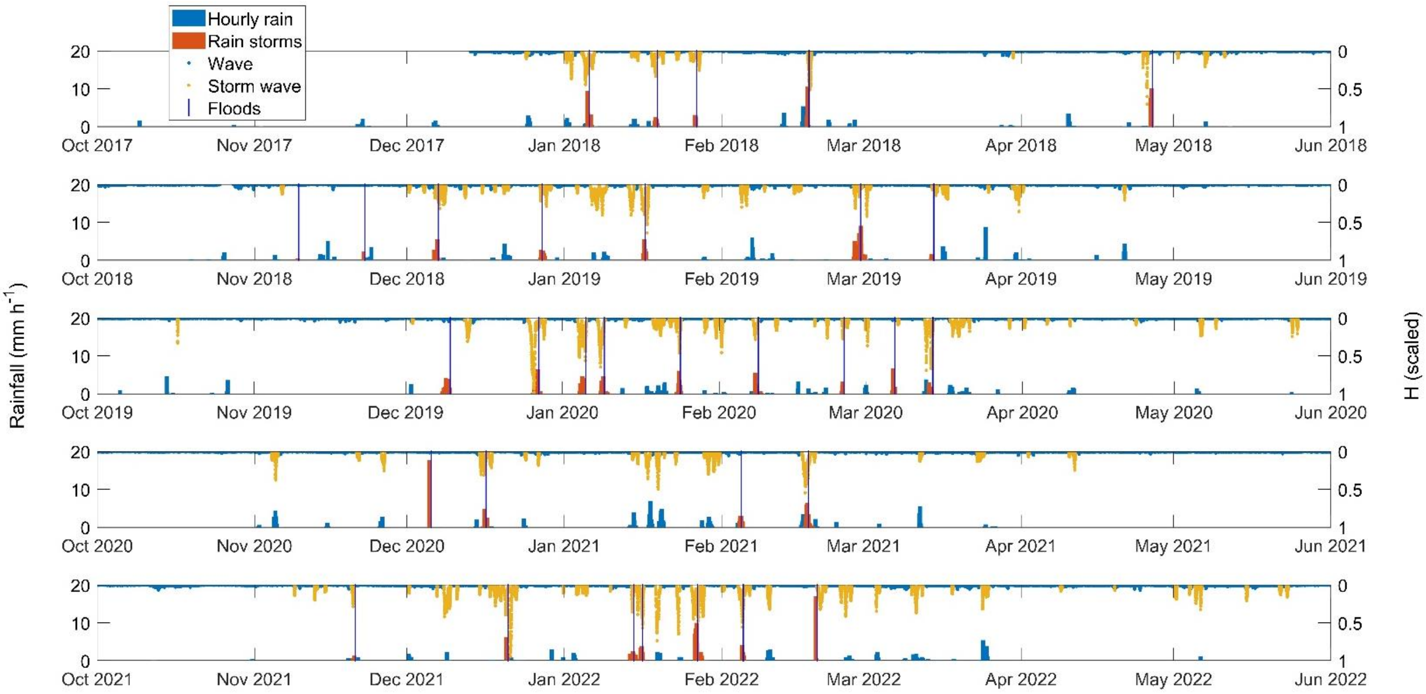

Figure 11: The interaction between fluvial and coastal conveyors during five consecutive hydrological years 2017-2022. Hourly rain depth measured in Ma'ale Adumim (location in Fig. 2b) with classified flood-producing rainstorms (left axis; blue and orange bars, respectively). Vertical blue lines represent the occurrence of floods (Table S1). Waves with classified storm waves (reversed, right-axis; blue and yellow dots, respectively).

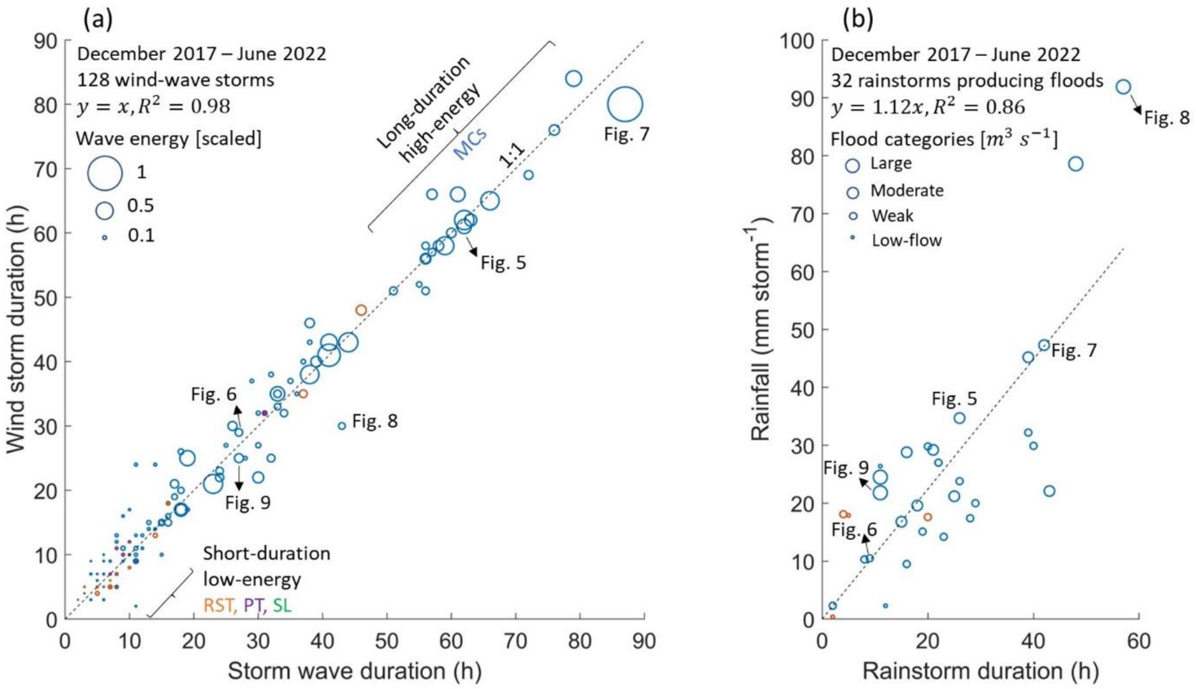

Figure 12: (a) Duration of wind versus wave storms (circles), the energy of a storm wave (circle size), and atmospheric CPs (MC-blue, RST-orange, PT-purple, SL-green). Storm wave energy was calculated for each storm according to $E{\sim}\sum H_{m0}^2$, and then scaled between 0 to 1 according to the full range of storm wave energies. (b) Rainfall depth versus rainstorm duration at rainstorms-producing floods (circles), the categories of floods (circle sizes), and CPs according to the same color coding as in (a).

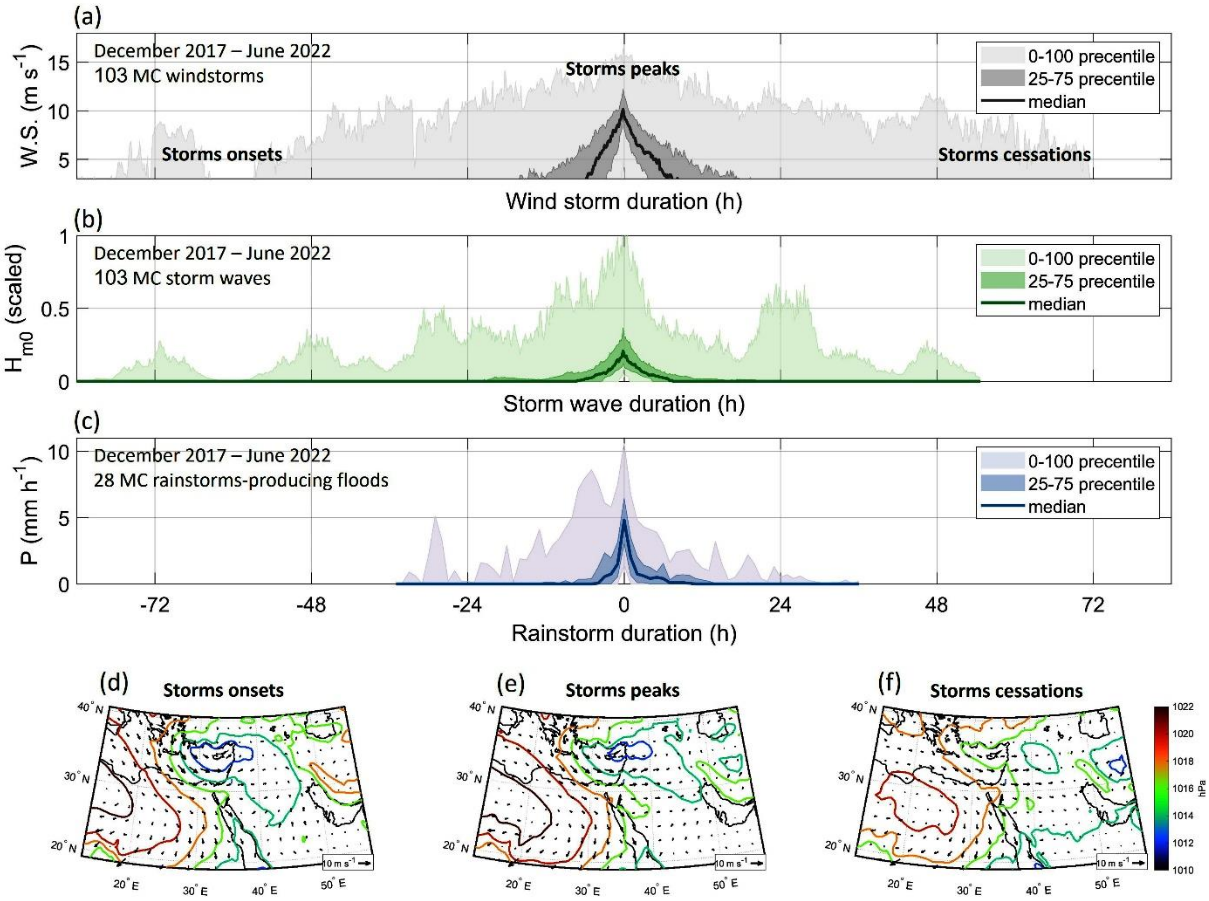

553 **Figure 13: The 'mean' (a) wind speed, (b) wave height, and (c) flood-producing rainstorms under MCs. Median storms**
554 **values (solid lines), intermediate quantiles of the storms (25-75%) and the full range of values (0-100%) is indicated**
555 **(shaded-colored areas). Composite mean pressure maps at the (d) onset, (e) peak, and (f) cessation of the wind-wave**
556 **storms showing the mean synoptic-scale evolution/climatology during the storms.**

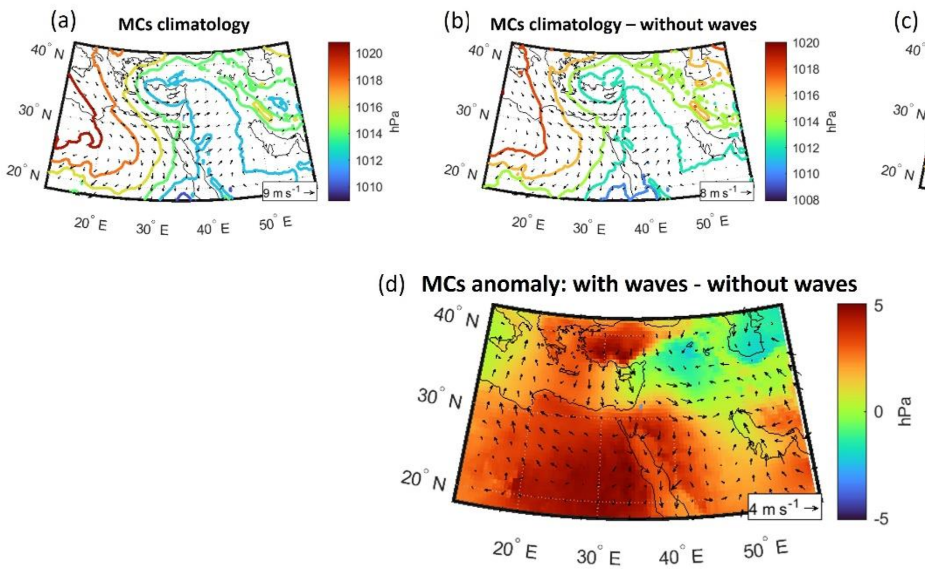

Figure 14: The climatology and anomaly of MCs producing and non-producing wind-wave storms. MCs climatology composite pressure maps of (a) all days classified as MC (following Alpert et al., 2004), (b) the non-generating wind-wave storms, (c) the generating wind-wave storms. (d) The difference (subtraction) between the generating and non-generating MCs.

5. Hydroclimatic signature in modern and paleo-sedimentary sequences

Following the detailed observations of waves, floods, and related sediment transport under Mediterranean low-pressure circulation patterns (MC, Sect. 4), we discuss here the accumulation and resulted architecture of modern and paleo-Dead Sea coastal landforms that were formed over time scales of decades to millennia, i.e., beyond the temporal scales of storms and seasons. In Sect. 5.1, we discuss the accumulation of the Nahal Og recent to modern coarse-delta environment while crossing the Dead Sea shelf and slope under rapid lake-level fall of the past decades. Then, Sect. 5.2 presents observations of a nearby stream and its coastal landforms which have accumulated on top of the shelf during the last modern Dead Sea highstand (late 19th to earliest 20th century). Finally, in Sect. 5.3, we use the gained insights in analyzing the map view of a Late Pleistocene coarse-clastic delta and its paleo-beach berms, which formed at the foot of the Dead Sea western escarpment.

5.1 The evolution of modern lowstand coastal berms at Nahal Og mouth

The coarse-clastic beach berms at the Nahal Og mouth have accumulated since the early 2000s (Eyal et al., 2019) (Fig. 2d), pointing to three sedimentary/architectural trends over time: (i) Northward downwind drift of clasts and the deposition of beach berms. (ii) An increase in the length of beach berms under action of storm-waves at the multi-annual scale. (iii) Berms show an increase in sediment volume and clast size along receding shorelines (Eyal et al., 2019 and Fig. 15). The northward orientation of deposition is attributed to the abovementioned MCs-generated winter storms and northward propagating waves. However, these trends of increased lengthening, volume, and grain-size cannot be explained by trends in the hydroclimatic forcing of winter rain-floods or by wind-waves; these two parameters do not exhibit a trend in the past decades (Sect. S2, Fig. 15d-e). If anything, a regional drying trend is proposed due to the poleward shift of the storm track and a decrease in total storm rainfall (e.g., Shohami et al., 2011; Zittis et al., 2022; Zappa et al., 2015; Hochman et al., 2018; Armon et al., 2022).

Therefore, the increase in sediment volume flux with time should represent intensified sediment delivery to the basin. This is attributed primarily to the steepening and incision of the channel in response to lake-level fall (Fig. 15b); it should be noted that the source of the coarse sediments is upstream without any sediment contribution by a littoral updrift. Following the emergence of the Dead Sea slope from underwater with its ~11% gradient (relatively constant since the late 1980s, Fig. 2d and 5c in Eyal et al., 2019), the channel mouth steepened and rapid incision across the shelf was triggered (Eyal et al., 2019). An expanding knickzone evolved with higher gradients migrating upstream (Ben Moshe et al., 2008), concurrently with channel deepening that should increase fluid shear stress exerted on the narrowing channel bed, and therefore, increased bedload sediment flux to the channel mouth (Meyer-Peter and Müller, 1948). Indeed, the transport rate across the shelf for a specific clast size increased over time from tens to hundreds of meters per year over ~15 years (see discussion regarding the 'virtual velocity' in Eyal et al., 2019). In larger spatiotemporal scales, it was shown that channel gradient is a first-order control on sediment supply to river mouths together with the contributing drainage area (Syvitski and Milliman, 2007). The latter factor is dominant along the global ocean shores during glacial periods when global sea level falls and watersheds may merge over the exposed continental shelf (Mulder and Syvitski, 1996; Burgess and Hovius, 1998), supplying larger volumes of sediment into a certain lowstand delta (e.g., Anderson et al., 2016, for the rivers draining into the Gulf of Mexico). The contribution of climate change during glacial lowstands is considered a second order influencer (Syvitski and Milliman, 2007), with complex relations that may result in either increase or decrease of the sediment delivery to channel mouths (e.g., Blum and Hattier-Womack, 2009) mainly of the suspended sediment fraction (e.g., Mulder and Syvitski, 1996; Fagherazzi et al., 2004).

The lengthening of beach berms with time under similar annual wave climate is a less clear phenomenon as it was concluded before that a single clast of a certain mass would travel a fixed, quite predictable distance under a given distribution of wave heights during a storm (Eyal et al., 2021). This raises the question: why would annually increasing sediment volumes travel farther along the shore under a similar wave climate? During the early 2000s, when small sediment volumes were delivered to the shore, beach berms of <100 m were formed (Fig. 2d, Fig. 15c), whereas between 2018-2022, larger sediment volumes were delivered to the shore and gravels were displaced longer distances of hundreds of meters along the shore during single storms (Figs. 5f, 9f). Three mechanisms may explain this observation: (i) Larger sediment volume accumulate up to shallower water depth and are subjected to higher near-surface wave\breaking-wave orbital velocities, relative to smaller sediment volumes on which lower fluid velocities are exerted at a deeper depth. Thus, the potential of gravels to travel longer distances along the shore is higher for larger sediment volume. (ii) The increased probability of a clast to be washed out of the swash zone during a storm coevally to the dominating stormy longshore transport (e.g., Benelli et al., 2012). Lighter/smaller clasts have a higher probability to be washed out of the swash zone than heavier/larger clasts that tend to travel down the beach slope under the influence of gravity (e.g., Grottoli et al., 2015). Consequently, smaller sediment volumes, characterized by smaller clast size distributions (Eyal et al., 2019), have a higher probability to be washed completely out of the swash zone at the early stages of the season, forming shorter-extending beach berms. (iii) Cross-shore down-slope flux of coarse sediments between beach berms of successive years. The lake level decline of ca. 1.2 m y^{-1} currently operates over the relatively steep, ~11%, beach slope, exposing annually ca. one half (10-15 m) of the 20-to-30-m wide strip of coarse sediments that are deposited alongshore. Thus, <50% of the coarse sediment remains submerged underwater with a potential to further move along the shore during the following winters. Such sediments start to move from an advanced downdrift location, reaching farther northward distances. This inter-annual cross-shore sediment flux is superimposed on the existing signal of increasing fluvial sediment volume flux conveyed to the coast with time.

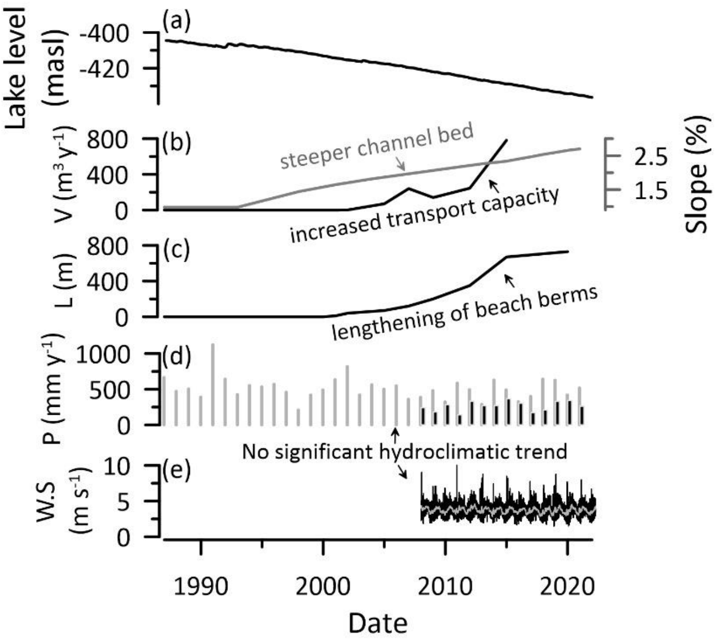

Figure 15: Reorganization and the buildup of lowstand sedimentary record under hydroclimatic forcing. (a) Dead Sea lake level. (b) Average channel slope of Nahal Og, measured between Highway 90 to the Dead Sea (Fig. 2c), increase with time in response to rapid level decline (right axis; grey), the estimated increase in annual volume flux of sediment (V) delivered to the channel mouth following Eyal et al., (2019) (left axis; black). (c) Increase in the length (L) of beach berms with time. (d) Annual rainfall (P) in Ma'ale Adumim (black bars, 2008-2022) and Jerusalem (grey bars, 1985-2022). (e) Wind speed (W.S) in Beit Ha'Arava (black line; daily mean, grey line; monthly mean, 2008-2022).

It was demonstrated that the plan-view sedimentation geometry and the channel orientation of wave-dominated deltas are controlled by feedbacks between the directional wave climate, fluvial sediment supply, and alongshore sediment bypassing (Nienhuis et al., 2016, their Figure 4); relatively low fluvial and littoral-updrift sediment supply support the asymmetry in the deposition of deltas with channels evolving in the downdrift direction. In the mouth of Nahal Og, alongshore transport by waves occurs over five times more frequently than the delivery of sediments by moderate and larger floods (Sect. 4), i.e., the potential longshore sediment transport is by far larger than the stream sediment input (Nienhuis et al., 2015); This indicates that a deltaic depocenter cannot evolve and the sediments are transported and deposited downdrift alongshore. We attribute the perpendicular alignment of the channel mouth with the shoreline (Figure 2d) to the absence of updrift sediment contribution. Additionally, according to Nienhuis et al. (2016), under constant wave climate (Fig. 15e) and an increase in the fluvial sediment supply (Fig. 15b), the deltaic\shorelines architecture should become more symmetric with time. However, continuous and rapid lake-level fall results in the separation of annually fluvially-derived sediment packages; instead of accumulating at the same elevation in front of the channel mouth with the shoreline changing its orientation, sediments are transported laterally away from the channel mouth and are deposited along individual shorelines at different elevations.

5.2 Modern highstand coastal landforms of a nearby stream (Nahal Qumeran)

The northward elongation of beach berms deposited during the highstand phase of the early 20th century Dead Sea at the mouth of a nearby ephemeral stream, Nahal Qumeran (Fig. 16a-c) provides a wider perspective of our analysis. The Nahal Qumeran catchment is neighboring Nahal Og from the south (Fig. 2b,c). It is smaller (47 km^2) and drier watershed with mean annual rain volume over its watershed of $8x10^6$ m^3 y^{-1} (Ben Moshe et al., 2008) is, by far, lower than the Nahal Og watershed that tap the wetter zone of the Judean mountains (Fig. 2). Between 1945 to 1960 the Dead Sea level was relatively stable, ranging between -390 to -395 mbsl, and Nahal Qumeran was fluvially connected to the Dead Sea shores through a braided coarse-clastic fan-delta. During the 1960s and 1970s, with the onset of human-induced lake-level decline, the stream was keeping pace with the slowly regressive shoreline to feed its highstand fan-delta (Fig. 16b,c). During this interval, a series of beach berms, similar to those observed in Nahal Og, were formed; these berms are also extended to the north from the Nahal Qumeran channel mouth, fitting the above-detected preferred directionality of winter winds and storm waves (Sect. 4). We do not identify any trends of increased sediment volumes or lengthening of beach berms in the channel mouth of the Nahal Qumeran, probably because its base level was quite stable and the channel profile and sediment flux were not interrupted. A change is noted at the early 1970s, when the lake-level decline has accelerated; at this stage, the Qumeran channel was not able to keep pace with the rapid receding shoreline and the low-gradient mudflats emerged (see also Eyal et al., 2019; Enzel et al., 2022). At that moment, Nahal Qumeran stopped responding to the rapid lake-level decline and disconnected from the lake, showing no incision across the shelf or any sediment delivery to the lake (Eyal et al., 2019). Instead, this stream maintains the buildup of an alluvial fan prograding onto the mudflat platform, without a noticeable impact by the lake coastal hydrodynamics that has generated the northward depositional asymmetry, related to the regional forcing of MCs. It seems that as long as the fluvial and coastal conveyors interacted at the Nahal Qumeran, regional hydroclimatology was manifested in northward elongating beach berms, similar to Nahal Og. However, disconnecting the fluvial from the coastal conveyors, transformed the channel mouth from a fan-delta into an alluvial fan that develops onto the mudflats regardless of the water body hydrodynamics.

5.3 Late Pleistocene Lake Lisan - sedimentary record of Nahal Tmarim

Following the observations from the modern Dead Sea in Nahal Og and Nahal Qumeran, we explore whether the control of southern winds along the Dead Sea rift valley, had affected past deltaic-coastal sedimentary morphology. At the foot of the western Dead Sea escarpment at stream outlets there are well-preserved, Gilbert-type fan-deltas, alluvial fans, and paleo-shorelines including beach berms that are associated with the higher stands of the Late Pleistocene Lake Lisan and its latest Pleistocene recession (Fig. 16a,d,e; see Fig 2b for the extent of Lake Lisan) (e.g., Manspeizer, 1985; Frostick and Reid, 1989; Bowman, 1971, 2019; Enzel et al., 2022). We have recognized a noticeable asymmetry in the deposition of fan-deltas and shoreline features at the exits of large and small streams from the northwestern Dead Sea escarpment; they present preferential deposition and more pronounced shorelines north (vs. south) of the feeding canyon mouths (Sect. S7). Channel outlets from the Dead Sea escarpment/cliff are basically bedrock canyons and, therefore, maintain their locations since the Late Pleistocene. Successions of Lake Lisan deposits are preserved inside deeply incised canyons at stream banks (e.g., Bartov et al., 2007) indicating this stable outlets. Thus, the depositional geometry and asymmetry of the channel deposits are evaluated with respect to the channel outlet from the Dead Sea escarpment as an indicator of their deposition due to funneled wind and wave storm direction in the Late Pleistocene. Here we present one example from the outlet of Nahal Tmarim (~22 km^2 drainage area), located ~15 km south of Nahal Og (Fig. 2b,c). Its Pleistocene fan-delta and its recessional paleo-shorelines/beach berms are deposited at elevations ranging between 310 to 350 mbsl, in part corresponding to Late Pleistocene to Holocene lake-level decline (e.g., Bartov et al., 2007; Torfstein and Enzel, 2017). The depositional configuration shows the abovementioned asymmetry, with most of the sediment volume of the fan-delta extends northward of the stream outlet from the cliff (Fig. 16d,e); the surface area of deposits north of the channel outlet is four times larger than the respective area south of the outlet. Furthermore, sorting of cobbles-boulders is observed along the paleo-shorelines of Nahal Tmarim, where clast size decreases northward and away from the Tmarim channel outlet, whereas, practically, no shorelines/berms are recognized south of the stream outlet. The present-day fan-delta of Nahal Tmarim is different from the modern fan-deltas of Nahal Og and Nahal Qumeran in several aspects: (i) It is a thick (20-30 m) deposit with Gilbert-type forests and paleo-shorelines, are preserved on its surface. (ii) There is some additional contribution of coarse materials to the coastal system either directly by the nearby cliff taluses or by local debris flows occurring under exceptionally heavy storms (David-Novak et al., 2004; Ahlborn et al., 2018). (iii) The Nahal Tmarim delta was built during Lake Lisan highstand but was also shaped during the regression of the lake and the transition into the Holocene (sometimes between 20-12 ka). Despite these dissimilarities, the framework under which this sedimentary record had evolved with the northward extension of the delta, seems similar. In both cases, modern and Late Pleistocene, observations agree with the domination of southern wind-wave regime and its signature in the morphology and sediment distribution.

The highest stand of Lake Lisan ca. 26,000 years ago reached 145-165 meters below sea level (Bowman and Gross, 1992; Bartov et al., 2002; Abu Ghazleh and Kempe, 2009), and extended over 240 km, from the Sea of Galilee to the northern Arava (e.g., Bartov 2007) (Fig. 2a). The potential length of the fetch, which currently encompass the length of the northern Dead Sea basin, but only for southerly winds, was much larger during the high stand for the current northern Dead Sea basin. This is correct for both northern and southern winds blowing into the study area from the northern and southern edges of Lake Lisan. Thus, both northerlies, presently driven by meso-scale circulation of Mediterranean Sea breeze (e.g., Lensky et al., 2018), and southerlies, mainly driven by synoptic-scale MCs, could have potentially generated waves high enough to transport gravels along the shores of the lake in both directions. However, the observed preferential deposition asymmetry points to the southerlies control, and in turn, to MCs that generated these southerlies-driven-waves with transport of coarse gravels northward; we did not identify evidence for a preferred fetch from the north.

Moreover, the northward directional organization of coarse sediments in the basin agrees with the increased frequency of MCs during wetter intervals of high lake stands in the Dead Sea basin (Armon et al., 2019; Enzel et al., 2003, 2008; Ben Dor et al., 2018). This inference is based on present-day climatology showing that wetter winters and high-lake levels are characterized by higher frequencies of deeper and southerly displaced storm tracks of MCs (e.g., Ben Dor et al., 2018; Enzel et al., 2008, 2003; Saaroni et al., 2010). Prevalence of more frequent, deeper MCs during the wetter Late Pleistocene, should have been resulted in an intensified activation of both the *fluvial* and *coastal sediment conveyors,* compared with modern conditions, as MC is the only CP that can generate both rainstorms and windstorms in this region. Floods were more intense and probably more frequent (Ben Dor et al., 2018), they have delivered amplified sediment fluxes into the basin (Bartov et al., 2007).

Westerlies/southwesterlies funneled in the rift valley into southerlies were more frequent and intensified, blowing over a longer lake fetch of diluted/fresher and less dense water, thus potentially generating higher amplitude waves, with heights that exceeded the maximum modern height of four meters. Such waves are characterized by higher fluid orbital velocities that generate higher forces capable of transporting larger boulders for longer distances along the coast.

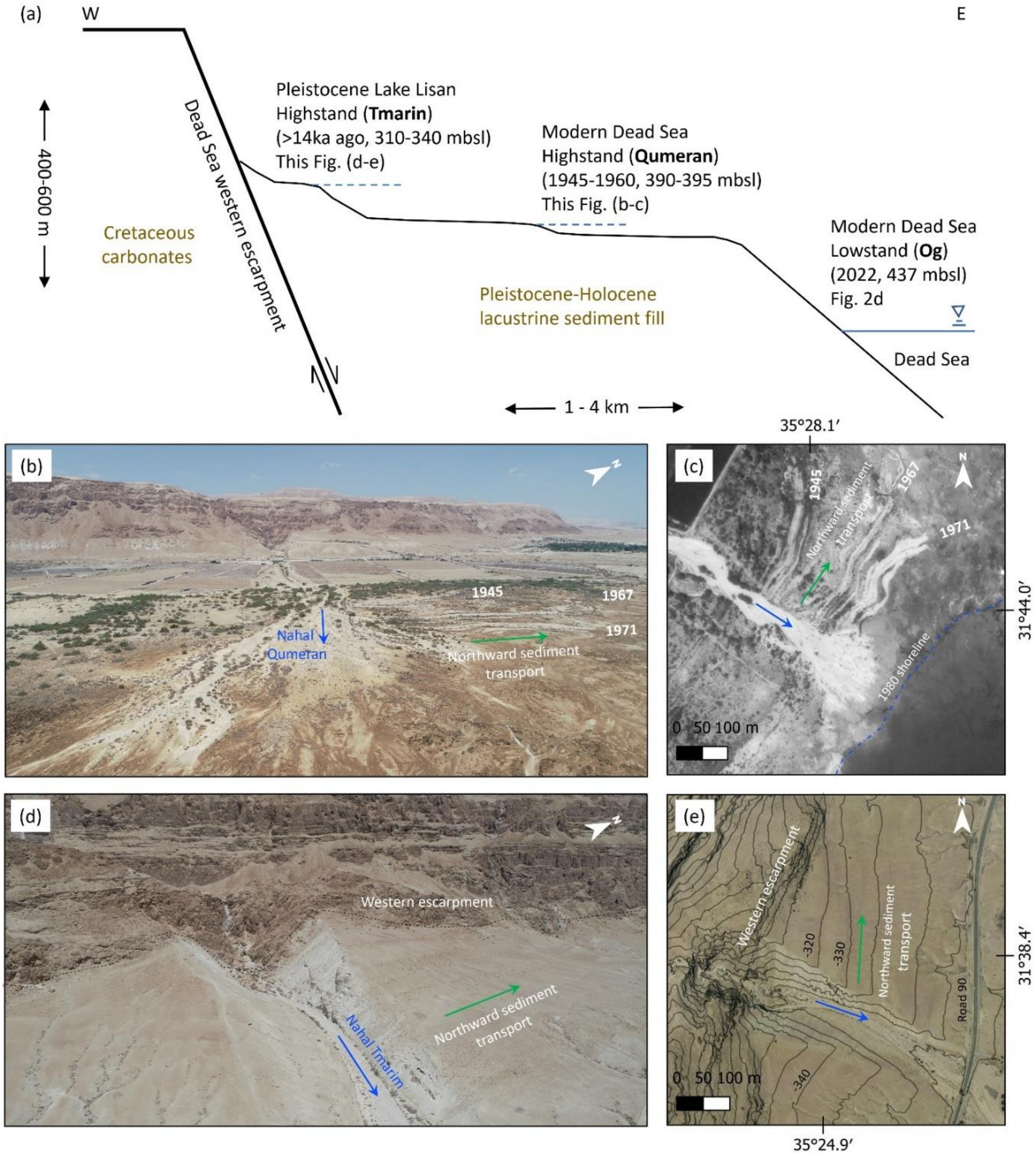

Figure 16: Modern and paleo-northward-extending beach berms and fan deltas. (a) Schematic cross section from the western Dead Sea escarpment to the modern Dead Sea showing the stratigraphic/geomorphic location of the three geomorphic records discussed in the paper. For location of the sites see Fig. 2b-c. (b) Angular drone photograph of Nahal Qumeran, and (c) orthophoto of Nahal Qumeran (1980), both showing the northward extending beach berms deposited as long as the stream fed the earlier 20th century shorelines with sediments. Since lake level decline has

accelerated, the stream did not keep pace with the receding shore and an alluvial fan begun developing on top of the exposed shelf. (d) Angular drone photograph of Nahal Tmarim, and (e) orthophoto of Nahal Tmarim (2012), both showing the norward deposition of fan-delta and beach berms under late Pleistocene Lake Lisan wind-wave regime. The asymmetry of sediment deposition to the north is evident also by looking at the elevation contours in (e), converging with steps of pleo-shorelines, with respect to the escarpment strike; northward of the channel, contours are sub-parallel to the escarpment direction, whereas they diagonally approach it on the southern part.

6. Summary and conclusions

Mediterranean cyclones (MCs) are the main synoptic-scale generators of both rain and storm waves over the Dead Sea region. Thus, they are also the main drivers for the coarse-clastic fluvial sediment flux into the lake and the transport and sorting of clasts along shores. First, these MCs generate the high-magnitude more persistent synoptic wind with westerly cyclonic circulation propagating to the northeastern Mediterranean. Near the surface and perpendicular to this synoptic wind direction, the flow is funneled topographically along the Dead Sea rift valley into southerlies that generate waves activating the *coastal conveyor*. Then, when the cyclone position migrates closer to the eastern Mediterranean shoreline or is centered inland over Syria, the northern component of the wind becomes more prominent, the southerly wave-producing winds decay, and rainfall evolves in the watershed over the Judean Desert. The rainfall generates floods, which activate the *fluvial conveyor* within a few hours. Thus, fluvial sediments reach the basin either coevally with or completely after the decay of the storm waves. Accordingly, the longshore transport and sorting often occurs during the next storm, usually within the same season, or infrequently, over the same cyclonic system.
MCs-producing waves are, on average, ~10 hPa deeper, generating southern winds of up to 20 m s^{-1} that last >10 hours. When the wind-driven waves are higher than 0.6 m, which is the threshold for transporting a 1-kg clast, the coastal conveyor is activated and gravelly beach berms are formed. When rainfall of >10 mm per storm accumulates at the center of the watershed, moderate or larger floods are likely to activate the fluvial conveyor.

Although both the stream and coast are usually activated under MCs, the transport under storm waves is >five times more frequent than the delivery of sediments by moderate or larger floods. This is geomorphologically noticeable in the wave-dominated fan-delta, transformed into regressive beach berms extending northward of the Nahal Og mouth. As the hydroclimatic parameters that characterized floods show no clear trend in recent decades, the increase of sediment volume and clast size delivered to the channel mouth during this interval, are attributed here to the response of the stream profile to base-level fall. The exposed stream mouth is steep and results in incising, steepening, and in increased bedload transport capacity. Concurrently, under rather constant wave climate, this increase in sediment discharge is associated with longer transportation distances of coarse gravels along the shore, and the increase of the beach berms length with time.

Guided by the observation from modern environments, we recognized a similar directionality in Late Pleistocene sedimentary deposition northward of canyon mouths in fan-deltas and coastal deposits. This may imply similar synoptic scale hydroclimatic drivers also in the past. This, in turn, implies that over past several millennia, MCs have played the major role in connecting fluvial delivery of coarse sediments, and their distribution in the lake and along its coasts.

7. Data availability

The data related to this work is available on Mendeley Data repository https://data.mendeley.com/drafts/65bhpwftrh (Eyal et al., 2022), and in Table S1 in the supplement. Rain gauge data were provided and pre-processed by the Israel Meteorological Service (https://ims.data.gov.il/; they are freely available in Hebrew only). ERA5 data can be downloaded from https://cds.climate.copernicus.eu (Hersbach et al., 2020). Flood reports from the years 2019-2022 were obtained from the Desert Floods Research Center (https://floods.org.il/english/; they are freely available in Hebrew only).

8. Video supplement

The videos related to this article are available on https://photos.app.goo.gl/rLysYEfoVSzyGdQo7.

9. Supplement link

10. Author contribution

HE, MA, and NGL conceptualized this work. The methodology was developed by HE, MA, and NGL. Data curation and formal analyses were performed by HE and MA. Funding was acquired by NGL, YE, and HE. NGL and YE supervised the work. HE wrote the original draft of this paper, which was reviewed and edited by all authors.

11. Competing interests

The authors declare that they have no conflict of interest.

12. Acknowledgements

This study was funded by the following grants: PI-NGL: ISF-1471/18, BSF-2018/035, NSF-BSF-2019/637; PI-YE: ISF-946/18. HE is grateful to the Azrieli Foundation for the Azrieli Fellowship. MA was supported by an ETH Zürich Postdoctoral Fellowship (Project No. 21-1 FEL-67), by the Stiftung für naturwissenschaftliche und technische Forschung and the ETH Zürich Foundation. We thank Vladimir Lyakhovsky, Eckart Meiburg, Efrat Morin and Itai Haviv for discussions and insights. We acknowledge Ziv Mor, Ido Sirota, Raanan Bodzin, Uri Malik and Hallel Lutzky for the assistance in the field and laboratory and Liran Ben Moshe for the drone photography. Dorita Rostkier-edelstein and Lida Shendrik are acknowledged for providing the updated synoptic classifications following Alpert et al., 2004, and Yoav Levi for sharing the large IMS datasets of rain and wind.

13. References

Abu Ghazleh, S. and Kempe, S.: Geomorphology of Lake Lisan terraces along the eastern coast of the Dead Sea, Jordan, Geomorphology, 108, 246–263, https://doi.org/10.1016/j.geomorph.2009.02.015, 2009.

Ahlborn, M., Armon, M., Ben Dor, Y., Neugebauer, I., Schwab, M. J., Tjallingii, R., Shoqeir, J. H., Morin, E., Enzel, Y., and Brauer, A.: Increased frequency of torrential rainstorms during a regional late Holocene eastern Mediterranean drought, Quat. Res., 89, 425–431, https://doi.org/10.1017/qua.2018.9, 2018.

Alpert, P. and Shay-El, Y.: The moisture source for the winter cyclones in the EM, Isr. Meteorol. Res. Pap., 5, 20–27, 1994.

Alpert, P. and Ziv, B.: The Sharav Cyclone: Observations and some theoretical considerations, J. Geophys. Res., 94, 18495, https://doi.org/10.1029/JD094iD15p18495, 1989.

Alpert, P., Neeman, B. U., and Shay-El, Y.: Climatological analysis of Mediterranean cyclones using ECMWF data, Tellus A Dyn. Meteorol. Oceanogr., 42, 65–77, https://doi.org/10.3402/tellusa.v42i1.11860, 1990a.

Alpert, P., Abramsky, R., and Neeman, B. U.: The prevailing summer synoptic system in Israel—subtropical high, not Persian trough, Isr. J. Earth Sci, 39, 93–102, 1990b.

Alpert, P., Shafir, H., and Issahary, D.: Recent changes in the climate at the Dead Sea–a preliminary study, Clim. Change, 37, 513–537, https://doi.org/https://doi.org/10.1023/A:1005330908974, 1997.

Alpert, P., Osetinsky, I., Ziv, B., and Shafir, H.: A new seasons definition based on classified daily synoptic systems: an example for the eastern Mediterranean, Int. J. Climatol., 24, 1013–1021, https://doi.org/10.1002/joc.1037, 2004a.

Alpert, P., Osetinsky, I., Ziv, B., and Shafir, H.: Semi-objective classification for daily synoptic systems: application to the eastern Mediterranean climate change, Int. J. Climatol., 24, 1001–1011, https://doi.org/10.1002/joc.1036, 2004b.

Amit, R. and Gerson, R.: The evolution of holocene reg (gravelly) soils in deserts: An example from the dead sea region, CATENA, 13, 59–79, https://doi.org/10.1016/S0341-8162(86)80005-4, 1986.

Anderson, J. B., Wallace, D. J., Simms, A. R., Rodriguez, A. B., Weight, R. W. R., and Taha, Z. P.: Recycling sediments between source and sink during a eustatic cycle: Systems of late Quaternary northwestern Gulf of Mexico Basin, Earth-Science Rev., 153, 111–138, https://doi.org/10.1016/j.earscirev.2015.10.014, 2016.

Arbel, S., Getker, M., Arazi, A., Yosi, B., Moshe, G., Efraim, F., and Alon, M.: Data of rain and floods of exceptional events in the hydrological year 2006-2007, special report M-84, 2009.

Armon, M., Dente, E., Smith, J. A., Enzel, Y., and Morin, E.: Synoptic-Scale Control over Modern Rainfall and Flood Patterns in the Levant Drylands with Implications for Past Climates, J. Hydrometeorol., 19, 1077–1096, https://doi.org/10.1175/JHM-D-18-0013.1, 2018.

Armon, M., Morin, E., and Enzel, Y.: Overview of modern atmospheric patterns controlling rainfall and floods into the Dead Sea: Implications for the lake's sedimentology and paleohydrology, Quat. Sci. Rev., 216, 58–73, https://doi.org/10.1016/j.quascirev.2019.06.005, 2019.

Armon, M., Marra, F., Enzel, Y., Rostkier-Edelstein, D., and Morin, E.: Radar-based characterisation of heavy precipitation in the eastern Mediterranean and its representation in a convection-permitting model, Hydrol. Earth Syst. Sci., 24, 1227–1249, https://doi.org/10.5194/hess-24-1227-2020, 2020.

Armon, M., Marra, F., Enzel, Y., Rostkier-Edelstein, D., Garfinkel, C. I., Adam, O., Dayan, U., and

Morin, E.: Reduced Rainfall in Future Heavy Precipitation Events Related to Contracted Rain Area Despite Increased Rain Rate, Earth's Futur., 10, e2021EF002397, https://doi.org/10.1029/2021EF002397, 2022.

Ashton, A. D. and Giosan, L.: Wave-angle control of delta evolution, Geophys. Res. Lett., 38, n/a-n/a, https://doi.org/10.1029/2011GL047630, 2011.

Ashton, A. D., Hutton, E. W. H., Kettner, A. J., Xing, F., Kallumadikal, J., Nienhuis, J., and Giosan, L.: Progress in coupling models of coastline and fluvial dynamics, Comput. Geosci., 53, 21–29, https://doi.org/10.1016/j.cageo.2012.04.004, 2013.

Bárdossy, A. and Filiz, F.: Identification of flood producing atmospheric circulation patterns, J. Hydrol., 313, 48–57, https://doi.org/10.1016/j.jhydrol.2005.02.006, 2005.

Bartov, Y., Stein, M., Enzel, Y., Agnon, A., and Reches, Z.: Lake Levels and Sequence Stratigraphy of Lake Lisan, the Late Pleistocene Precursor of the Dead Sea, Quat. Res., 57, 9–21, https://doi.org/10.1006/qres.2001.2284, 2002.

Bartov, Y., Goldstein, S. L., Stein, M., and Enzel, Y.: Catastrophic arid episodes in the Eastern Mediterranean linked with the North Atlantic Heinrich events, Geology, 31, 439, https://doi.org/10.1130/0091-7613(2003)031<0439:CAEITE>2.0.CO;2, 2003.

Bartov, Y., Bookman, R., and Enzel, Y.: Current depositional environments at the Dead Sea margins as indicators of past lake levels, in: New Frontiers in Dead Sea Paleoenvironmental Research, vol. 401, Geological Society of America, 127–140, https://doi.org/10.1130/2006.2401(08), 2006.

Bartov, Y., Enzel, Y., Porat, N., and Stein, M.: Evolution of the Late Pleistocene Holocene Dead Sea Basin from Sequence Statigraphy of Fan Deltas and Lake-Level Reconstruction, J. Sediment. Res., 77, 680–692, https://doi.org/10.2110/jsr.2007.070, 2007.

Belachsen, I., Marra, F., Peleg, N., and Morin, E.: Convective rainfall in a dry climate: relations with synoptic systems and flash-flood generation in the Dead Sea region, Hydrol. Earth Syst. Sci., 21, 5165–5180, https://doi.org/10.5194/hess-21-5165-2017, 2017.

Benelli, G., Pozzebon, A., Bertoni, D., and Sarti, G.: An RFID-Based Toolbox for the Study of Under- and Outside-Water Movement of Pebbles on Coarse-Grained Beaches, IEEE J. Sel. Top. Appl. Earth Obs. Remote Sens., 5, 1474–1482, https://doi.org/10.1109/JSTARS.2012.2196499, 2012.

Ben Dor, Y., Armon, M., Ahlborn, M., Morin, E., Erel, Y., Brauer, A., Schwab, M. J., Tjallingii, R., and Enzel, Y.: Changing flood frequencies under opposing late Pleistocene eastern Mediterranean climates, Sci. Rep., 8, 8445, https://doi.org/10.1038/s41598-018-25969-6, 2018.

Ben Moshe, L., Haviv, I., Enzel, Y., Zilberman, E., and Matmon, A.: Incision of alluvial channels in response to a continuous base level fall: Field characterization, modeling, and validation along the Dead Sea, Geomorphology, 93, 524–536, https://doi.org/10.1016/j.geomorph.2007.03.014, 2008.

Bitan, A.: The wind regime in the north-west section of the Dead-Sea, Arch. für Meteorol. Geophys. und Bioklimatologie Ser. B, 22, 313–335, https://doi.org/10.1007/BF02246585, 1974.

Bitan, A.: The influence of the special shape of the dead-sea and its environment on the local wind system, Arch. für Meteorol. Geophys. und Bioklimatologie Ser. B, 24, 283–301, https://doi.org/10.1007/BF02263460, 1976.

Blum, M. D., Martin, J., Milliken, K., and Garvin, M.: Paleovalley systems: Insights from Quaternary analogs and experiments, Earth-Science Rev., 116, 128–169, https://doi.org/10.1016/j.earscirev.2012.09.003, 2013.

Blum, M. D. and Hattier-Womack, J.: Climate Change, Sea-Level Change, and Fluvial Sediment Supply to Deepwater Depositional Systems, in: External Controls of Deep-Water Depositional Systems, SEPM (Society for Sedimentary Geology), 15–39, https://doi.org/10.2110/sepmsp.092.015, 2009.

Bookman, R., Enzel, Y., Agnon, A., and Stein, M.: Late Holocene lake levels of the Dead Sea, Geol. Soc. Am. Bull., 116, 555–571, https://doi.org/https://doi.org/10.1130/B25286.1, 2004.

Bookman, R., Bartov, Y., Enzel, Y., and Stein, M.: Quaternary lake levels in the Dead Sea basin: two centuries of research, Geol. Soc. Am. Spacial Pap., 401, 155–170, https://doi.org/10.1130/2006.2401(10).For, 2006.

Borga, M., Comiti, F., Ruin, I., and Marra, F.: Forensic analysis of flash flood response, WIREs Water, 6, e1338, https://doi.org/10.1002/wat2.1338, 2019.

Bowman, D.: Geomorphology of the shore terraces of the late pleistocene Lisan lake (Israel), Palaeogeogr. Palaeoclimatol. Palaeoecol., 9, 183–209, https://doi.org/10.1016/0031-0182(71)90031-9, 1971.

Bowman, D.: The Regional Approach: Alluvial Fans along the Dead Sea-Arava Rift Valley, in: Principles of Alluvial Fan Morphology, Springer Netherlands, Dordrecht, 135–151, https://doi.org/10.1007/978-94-024-1558-2_19, 2019.

Bowman, D. and Gross, T.: The highest stand of Lake Lisan:∼ 150 meter below MSL, Isr. J. Earth-Sciences, 41, 233–237, 1992.

Bowman, D., Banet-Davidovich, D., Bruins, H. J., and Plicht, J. Van der: Dead Sea shoreline facies with seismically-induced soft-sediment deformation structures, Israel, Isr. J. Earth Sci., 49, 197–214, https://doi.org/10.1560/GXHT-AK5W-46EF-VTR8, 2000.

Bowman, D., Svoray, T., Devora, S., Shapira, I., and Laronne, J. B.: Geomorphology Extreme rates of channel incision and shape evolution in response to a continuous , rapid base-level fall , the Dead Sea , Israel, Geomorphology, 114, 227–237, https://doi.org/10.1016/j.geomorph.2009.07.004, 2010.

Bridge, J. S.: The interaction between channel geometry, water flow, sediment transport and deposition in braided rivers, Geol. Soc. London, Spec. Publ., 75, 13–71, https://doi.org/10.1144/GSL.SP.1993.075.01.02, 1993.

Burgess, P. M. and Hovius, N.: Rates of delta progradation during highstands: consequences for timing of deposition in deep-marine systems, J. Geol. Soc. London., 155, 217–222, https://doi.org/10.1144/gsjgs.155.2.0217, 1998.

Coleman, J. M. and Prior, D. B.: Deltaic environments of deposition, in: M 31: Sandstone Depositional Environments, AAPG Special Volumes, 139–178, 1982.

David-Novak, H. Ben, Morin, E., and Enzel, Y.: Modern extreme storms and the rainfall thresholds for initiating debris flows on the hyperarid western escarpment of the Dead Sea, Israel, Geol. Soc. Am. Bull., 116, 718, https://doi.org/10.1130/B25403.2, 2004.

Dayan, U. and Morin, E.: Flash flood–producing rainstorms over the Dead Sea: A review, in: New Frontiers in Dead Sea Paleoenvironmental Research, vol. 401, Geological Society of America, 53–62, https://doi.org/10.1130/2006.2401(04), 2006.

Dayan, U., Ricaud, P., Zbinden, R., and Dulac, F.: Atmospheric pollution over the eastern Mediterranean during summer – a review, Atmos. Chem. Phys., 17, 13233–13263, https://doi.org/10.5194/acp-

17-13233-2017, 2017.

Dayan, U., Lensky, I. M., Ziv, B., and Khain, P.: Atmospheric conditions leading to an exceptional fatal flash flood in the Negev Desert, Israel, Nat. Hazards Earth Syst. Sci., 21, 1583–1597, https://doi.org/10.5194/nhess-21-1583-2021, 2021.

Dente, E., Lensky, N. G., Morin, E., Grodek, T., Sheffer, N. A., and Enzel, Y.: Geomorphic Response of a Low-Gradient Channel to Modern, Progressive Base-Level Lowering: Nahal HaArava, the Dead Sea, J. Geophys. Res. Earth Surf., 122, 2468–2487, https://doi.org/10.1002/2016JF004081, 2017.

Dente, E., Lensky, N. G., Morin, E., Dunne, T., and Enzel, Y.: Sinuosity evolution along an incising channel: New insights from the Jordan River response to the Dead Sea level fall, Earth Surf. Process. Landforms, https://doi.org/10.1002/esp.4530, 2018.

Dente, E., Lensky, N. G., Morin, E., and Enzel, Y.: From straight to deeply incised meandering channels: Slope impact on sinuosity of confined streams, Earth Surf. Process. Landforms, 46, 1041–1054, https://doi.org/10.1002/esp.5085, 2021.

Elliot, T.: Deltas, edited by: Reading, H., Oxford, 113–154 pp., 1986.

Enzel, Y. and Bar-Yosef, O.: Quaternary of the Levant, edited by: Enzel, Y. and Bar-Yosef, O., Cambridge University Press, https://doi.org/10.1017/9781316106754, 2017.

Enzel, Y., Bookman, R., Sharon, D., Gvirtzman, H., Dayan, U., Ziv, B., and Stein, M.: Late Holocene climates of the Near East deduced from Dead Sea level variations and modern regional winter rainfall, Quat. Res., 60, 263–273, https://doi.org/10.1016/j.yqres.2003.07.011, 2003.

Enzel, Y., Agnon, A., and Stein, M.: New Frontiers in Dead Sea Paleoenvironmental Research, Geological Society of America, https://doi.org/10.1130/SPE401, 2006.

Enzel, Y., Amit, R., Dayan, U., Crouvi, O., Kahana, R., Ziv, B., and Sharon, D.: The climatic and physiographic controls of the eastern Mediterranean over the late Pleistocene climates in the southern Levant and its neighboring deserts, Glob. Planet. Change, 60, 165–192, https://doi.org/10.1016/j.gloplacha.2007.02.003, 2008.

Enzel, Y., Mushkin, A., Groisman, M., Calvo, R., Eyal, H., and Lensky, N.: The modern wave-induced coastal staircase morphology along the western shores of the Dead Sea, Geomorphology, 408, 108237, https://doi.org/10.1016/j.geomorph.2022.108237, 2022.

Eyal, H., Dente, E., Haviv, I., Enzel, Y., Dunne, T., and Lensky, N. G.: Fluvial incision and coarse gravel redistribution across the modern Dead Sea shelf as a result of base-level fall, Earth Surf. Process. Landforms, 44, 2170–2185, https://doi.org/10.1002/esp.4640, 2019.

Eyal, H., Enzel, Y., Meiburg, E., Vowinckel, B., and Lensky, N. G.: How Does Coastal Gravel Get Sorted Under Stormy Longshore Transport?, Geophys. Res. Lett., 48, e2021GL095082, https://doi.org/10.1029/2021GL095082, 2021.

Eyal, H., Armon, M., Enzel, Y., and Lensky, N. G.: Synoptic- to meso-scale circulation connects fluvial and coastal gravel conveyors and directional deposition of coastal landforms in the Dead Sea basin, Mendeley Data, V1, https://doi.org/10.17632/65bhpwftrh.1, 2022.

Fagherazzi, S.: Modeling fluvial erosion and deposition on continental shelves during sea level cycles, J. Geophys. Res., 109, F03010, https://doi.org/10.1029/2003JF000091, 2004.

Frostick, L. E. and Reid, I. A. N.: Climatic versus tectonic controls of fan sequences: lessons from the

Dead Sea, Israel, J. Geol. Soc. London., 146, 527–538, https://doi.org/10.1144/gsjgs.146.3.0527, 1989.

Galloway, W. E.: Process framework for describing the morphologic and stratigraphic evolution of deltaic depositional systems, 87–98, 1975.

Garfunkel, Z. and Ben-Avraham, Z.: The structure of the Dead Sea basin, Tectonophysics, 266, 155–176, https://doi.org/10.1016/S0040-1951(96)00188-6, 1996.

Gertman, I. and Hecht, A.: The Dead Sea hydrography from 1992 to 2000, J. Mar. Syst., 35, 169–181, https://doi.org/10.1016/S0924-7963(02)00079-9, 2002.

Goldreich, Y.: The spatial distribution of annual rainfall in Israel ? a review, Theor. Appl. Climatol., 50, 45–59, https://doi.org/10.1007/BF00864902, 1994.

Goldreich, Y.: The Climate of Israel, Springer US, Boston, MA, https://doi.org/10.1007/978-1-4615-0697-3, 2003.

Goldreich, Y., Mozes, H., and Rosenfeld, D.: Radar analysis of cloud systems and their rainfall yield in Israel, Isr. J. Earth Sci, 53, 63–76, 2004.

Goodwin, I. D., Mortlock, T. R., and Browning, S.: Tropical and extratropical-origin storm wave types and their influence on the East Australian longshore sand transport system under a changing climate, J. Geophys. Res. Ocean., 121, 4833–4853, https://doi.org/10.1002/2016JC011769, 2016.

Graf, M., Sprenger, M., Lohmann, U., Seibt, C., and Hofmann, H.: Evaluating the suitability of the SWAN/COSMO-2 model system to simulate short-crested surface waves for a narrow lake with complex bathymetry, Meteorol. Zeitschrift, 22, 257–272, https://doi.org/10.1127/0941-2948/2013/0442, 2013.

Grosse, G., Schirrmeister, L., Kunitsky, V. V, and Hubberten, H.: The use of CORONA images in remote sensing of periglacial geomorphology: an illustration from the NE Siberian coast, Permafr. Periglac. Process., 16, 163–172, https://doi.org/10.1002/ppp.509, 2005.

Grottoli, E., Bertoni, D., Ciavola, P., and Pozzebon, A.: Short term displacements of marked pebbles in the swash zone: Focus on particle shape and size, Mar. Geol., 367, 143–158, https://doi.org/10.1016/j.margeo.2015.06.006, 2015.

Hamdani, I., Assouline, S., Tanny, J., Lensky, I. M., Gertman, I., Mor, Z., and Lensky, N. G.: Seasonal and diurnal evaporation from a deep hypersaline lake: The Dead Sea as a case study, J. Hydrol., 562, 155–167, https://doi.org/10.1016/j.jhydrol.2018.04.057, 2018.

Hansford, M. R. and Plink-Björklund, P.: River discharge variability as the link between climate and fluvial fan formation, Geology, 48, 952–956, https://doi.org/10.1130/G47471.1, 2020.

Haviv, I.: Mechanics, morphology and evolution of vertical knickpoints (waterfalls) along the bedrock channels of the Dead Sea western tectonic escarpment, The Hebrew University of Jerusalem, 2007.

Hersbach, H., Bell, B., Berrisford, P., Hirahara, S., Horányi, A., Muñoz-Sabater, J., Nicolas, J., Peubey, C., Radu, R., Schepers, D., Simmons, A., Soci, C., Abdalla, S., Abellan, X., Balsamo, G., Bechtold, P., Biavati, G., Bidlot, J., Bonavita, M., Chiara, G., Dahlgren, P., Dee, D., Diamantakis, M., Dragani, R., Flemming, J., Forbes, R., Fuentes, M., Geer, A., Haimberger, L., Healy, S., Hogan, R. J., Hólm, E., Janisková, M., Keeley, S., Laloyaux, P., Lopez, P., Lupu, C., Radnoti, G., Rosnay, P., Rozum, I., Vamborg, F., Villaume, S., and Thépaut, J.: The ERA5 global reanalysis, Q. J. R. Meteorol. Soc., 146, 1999–2049, https://doi.org/10.1002/qj.3803, 2020.

Hochman, A., Mercogliano, P., Alpert, P., Saaroni, H., and Bucchignani, E.: High-resolution projection of climate change and extremity over Israel using COSMO-CLM, Int. J. Climatol., 38, 5095–5106, https://doi.org/10.1002/joc.5714, 2018.

Huntington, E.: Palestine and its Transformation, Houghton Mifflin, 1911.

Kahana, R., Ziv, B., Enzel, Y., and Dayan, U.: Synoptic climatology of major floods in the Negev Desert, Israel, Int. J. Climatol., 22, 867–882, https://doi.org/10.1002/joc.766, 2002.

Karimpour, A. and Chen, Q.: Wind wave analysis in depth limited water using OCEANLYZ, A MATLAB toolbox, Comput. Geosci., 106, 181–189, https://doi.org/10.1016/j.cageo.2017.06.010, 2017.

Kiro, Y., Goldstein, S. L., Garcia-Veigas, J., Levy, E., Kushnir, Y., Stein, M., and Lazar, B.: Relationships between lake-level changes and water and salt budgets in the Dead Sea during extreme aridities in the Eastern Mediterranean, Earth Planet. Sci. Lett., 464, 211–226, https://doi.org/10.1016/j.epsl.2017.01.043, 2017.

Kunin, P., Alpert, P., and Rostkier-Edelstein, D.: Investigation of sea-breeze/foehn in the Dead Sea valley employing high resolution WRF and observations, Atmos. Res., 229, 240–254, https://doi.org/10.1016/j.atmosres.2019.06.012, 2019.

Kushnir, Y., Dayan, U., Ziv, B., Morin, E., and Enzel, Y.: Climate of the Levant, in: Quaternary of the Levant, Cambridge University Press, 31–44, https://doi.org/10.1017/9781316106754.004, 2017.

Lekach, J. and Enzel, Y.: Flood-duration-integrated stream power and frequency magnitude of >50-year-long sediment discharge out of a hyperarid watershed, Earth Surf. Process. Landforms, 46, 1348–1362, https://doi.org/10.1002/esp.5104, 2021.

Lensky, I. M. and Dayan, U.: Continuous detection and characterization of the Sea Breeze in clear sky conditions using Meteosat Second Generation, Atmos. Chem. Phys., 12, 6505–6513, https://doi.org/10.5194/acp-12-6505-2012, 2012.

Lensky, I. M. and Dayan, U.: Satellite observations of land surface temperature patterns induced by synoptic circulation, Int. J. Climatol., 35, 189–195, https://doi.org/10.1002/joc.3971, 2015.

Lensky, N. G., Dvorkin, Y., Lyakhovsky, V., Gertman, I., and Gavrieli, I.: Water, salt, and energy balances of the Dead Sea, Water Resour. Res., 41, 1–13, https://doi.org/10.1029/2005WR004084, 2005.

Lensky, N. G., Lensky, I. M., Peretz, A., Gertman, I., Tanny, J., and Assouline, S.: Diurnal Course of Evaporation From the Dead Sea in Summer: A Distinct Double Peak Induced by Solar Radiation and Night Sea Breeze, Water Resour. Res., 54, 150–160, https://doi.org/10.1002/2017WR021536, 2018.

Longuet-Higgins, M. S.: Longshore currents generated by obliquely incident sea waves: 1, J. Geophys. Res., 75, 6778–6789, 1970.

Manspeizer, W.: The Dead Sea Rift: Impact of climate and tectonism on Pleistocene and Holocene sedimentation, 1985.

Marra, F. and Morin, E.: Autocorrelation structure of convective rainfall in semiarid-arid climate derived from high-resolution X-Band radar estimates, Atmos. Res., 200, 126–138, https://doi.org/10.1016/j.atmosres.2017.09.020, 2018.

Marra, F., Borga, M., and Morin, E.: A Unified Framework for Extreme Subdaily Precipitation Frequency Analyses Based on Ordinary Events, Geophys. Res. Lett., 47, e2020GL090209, https://doi.org/10.1029/2020GL090209, 2020.

Marra, F., Armon, M., Adam, O., Zoccatelli, D., Gazal, O., Garfinkel, C. I., Rostkier-Edelstein, D., Dayan, U., Enzel, Y., and Morin, E.: Toward Narrowing Uncertainty in Future Projections of Local Extreme

Precipitation, Geophys. Res. Lett., 48, e2020GL091823, https://doi.org/10.1029/2020GL091823, 2021.

Marra, F., Armon, M., and Morin, E.: Coastal and orographic effects on extreme precipitation revealed by weather radar observations, Hydrol. Earth Syst. Sci., 26, 1439–1458, https://doi.org/10.5194/hess-26-1439-2022, 2022.

Masselink, G., Scott, T., Poate, T., Stokes, C., Wiggins, M., Valiente, N., and Konstantinou, A.: Tale of two beaches: correlation between decadal beach dynamics and climate indices, in: Coastal Sediments 2023: The Proceedings of the Coastal Sediments 2023, World Scientific, 337–350, https://doi.org/https://doi.org/10.1142/9789811275135_0031, 2023.

Meadows, G. A., Meadows, L. A., Wood, W. L., Hubertz, J. M., and Perlin, M.: The Relationship between Great Lakes Water Levels, Wave Energies, and Shoreline Damage, Bull. Am. Meteorol. Soc., 78, 675–682, https://doi.org/10.1175/1520-0477(1997)078<0675:TRBGLW>2.0.CO;2, 1997.

Merz, B., Blöschl, G., Vorogushyn, S., Dottori, F., Aerts, J. C. J. H., Bates, P., Bertola, M., Kemter, M., Kreibich, H., Lall, U., and Macdonald, E.: Causes, impacts and patterns of disastrous river floods, Nat. Rev. Earth Environ., 2, 592–609, https://doi.org/10.1038/s43017-021-00195-3, 2021.

Meyer-Peter, E. and Müller, R.: Formulas for bed-load transport, in: IAHSR 2nd meeting, Stockholm, appendix 2, 1948.

Molina, R., Manno, G., Lo Re, C., Anfuso, G., and Ciraolo, G.: Storm Energy Flux Characterization along the Mediterranean Coast of Andalusia (Spain), Water, 11, 509, https://doi.org/10.3390/w11030509, 2019.

Montgomery, D. R. and Buffington, J. M.: Channel-reach morphology in mountain drainage basins, Bull. Geol. Soc. Am., 109, 596–611, https://doi.org/10.1130/0016-7606(1997)109<0596:CRMIMD>2.3.CO;2, 1997.

Morin, E., Jacoby, Y., Navon, S., and Bet-Halachmi, E.: Towards flash-flood prediction in the dry Dead Sea region utilizing radar rainfall information, Adv. Water Resour., 32, 1066–1076, https://doi.org/10.1016/j.advwatres.2008.11.011, 2009.

Mulder, T. and Syvitski, J. P. M.: Climatic and Morphologic Relationships of Rivers: Implications of Sea-Level Fluctuations on River Loads, J. Geol., 104, 509–523, https://doi.org/10.1086/629849, 1996.

Naor, R., Potchter, O., Shafir, H., and Alpert, P.: An observational study of the summer Mediterranean Sea breeze front penetration into the complex topography of the Jordan Rift Valley, Theor. Appl. Climatol., 127, 275–284, https://doi.org/10.1007/s00704-015-1635-3, 2017.

Neev, D. and Emery, K. O.: The Dead Sea: depositional processes and environments of evaporites, 1967.

Neugebauer, I., Schwab, M. J., Waldmann, N. D., Tjallingii, R., Frank, U., Hadzhiivanova, E., Naumann, R., Taha, N., Agnon, A., Enzel, Y., and Brauer, A.: Hydroclimatic variability in the Levant during the early last glacial (∼117–75 ka) derived from micro-facies analyses of deep Dead Sea sediments, Clim. Past, 12, 75–90, https://doi.org/10.5194/cp-12-75-2016, 2016.

Nienhuis, J. H., Ashton, A. D., and Giosan, L.: What makes a delta wave-dominated?, Geology, 43, 511–514, https://doi.org/https://doi.org/10.1130/G36518.1, 2015.

Nienhuis, J. H., Ashton, A. D., and Giosan, L.: Littoral steering of deltaic channels, Earth Planet. Sci. Lett., 453, 204–214, https://doi.org/10.1016/j.epsl.2016.08.018c, 2016.

Palchan, D., Neugebauer, I., Amitai, Y., Waldmann, N. D., Schwab, M. J., Dulski, P., Brauer, A., Stein, M., Erel, Y., and Enzel, Y.: North Atlantic controlled depositional cycles in MIS 5e layered sediments from the deep Dead Sea basin, Quat. Res., 87, 168–179, https://doi.org/10.1017/qua.2016.10, 2017.

Postma, G.: An analysis of the variation in delta architecture, Terra Nov., 2, 124–130, https://doi.org/10.1111/j.1365-3121.1990.tb00052.x, 1990.

Postma, G.: Sea-level-related architectural trends in coarse-grained delta complexes, Sediment. Geol., 98, 3–12, https://doi.org/10.1016/0037-0738(95)00024-3, 1995.

Pringle, J. and Stretch, D. D.: On a new statistical wave generator based on atmospheric circulation patterns and its applications to coastal shoreline evolution, Comput. Geosci., 149, 104707, https://doi.org/10.1016/j.cageo.2021.104707, 2021.

Pringle, J., Stretch, D. D., and Bárdossy, A.: Automated classification of the atmospheric circulation patterns that drive regional wave climates, Nat. Hazards Earth Syst. Sci., 14, 2145–2155, https://doi.org/10.5194/nhess-14-2145-2014, 2014.

Pringle, J., Stretch, D. D., and Bárdossy, A.: On linking atmospheric circulation patterns to extreme wave events for coastal vulnerability assessments, Nat. Hazards, 79, 45–59, https://doi.org/10.1007/s11069-015-1825-4, 2015.

Reid, I., Frostick, L. E., and Layman, J. T.: The incidence and nature of bedload transport during flood flows in coarse-grained alluvial channels, Earth Surf. Process. Landforms, 10, 33–44, https://doi.org/10.1002/esp.3290100107, 1985.

Rinat, Y., Marra, F., Armon, M., Metzger, A., Levi, Y., Khain, P., Vadislavsky, E., Rosensaft, M., and Morin, E.: Hydrometeorological analysis and forecasting of a 3 d flash-flood-triggering desert rainstorm, Nat. Hazards Earth Syst. Sci., 21, 917–939, https://doi.org/10.5194/nhess-21-917-2021, 2021.

Rodwell, M. J. and Hoskins, B. J.: Monsoons and the dynamics of deserts, Q. J. R. Meteorol. Soc., 122, 1385–1404, https://doi.org/10.1002/qj.49712253408, 1996.

Saaroni, H., Ziv, B., Bitan, A., and Alpert, P.: Easterly Wind Storms over Israel, Theor. Appl. Climatol., 59, 61–77, https://doi.org/10.1007/s007040050013, 1998.

Saaroni, H., Halfon, N., Ziv, B., Alpert, P., and Kutiel, H.: Links between the rainfall regime in Israel and location and intensity of Cyprus lows, Int. J. Climatol., 30, 1014–1025, https://doi.org/10.1002/joc.1912, 2010.

Segal, M., Mahrer, Y., and Pielke, R. A.: A study of meteorological patterns associated with a lake confined by mountains–the Dead Sea case, Q. J. R. Meteorol. Soc., 109, 549–564, 1983.

Sharon, D.: The spottiness of rainfall in a desert area, J. Hydrol., 17, 161–175, https://doi.org/10.1016/0022-1694(72)90002-9, 1972.

Sharon, D. and Kutiel, H.: The distribution of rainfall intensity in Israel, its regional and seasonal variations and its climatological evaluation, J. Climatol., 6, 277–291, https://doi.org/10.1002/joc.3370060304, 1986.

Shentsis, I., Laronne, J. B., and Alpert, P.: Red Sea Trough flood events in the Negev, Israel (1964–2007), Hydrol. Sci. J., 57, 42–51, https://doi.org/10.1080/02626667.2011.636922, 2012.

Shohami, D., Dayan, U., and Morin, E.: Warming and drying of the eastern Mediterranean: Additional evidence from trend analysis, J. Geophys. Res. Atmos., 116, n/a-n/a, https://doi.org/10.1029/2011JD016004, 2011.

Sirota, I., Enzel, Y., Mor, Z., Ben Moshe, L., Eyal, H., Lowenstein, T. K., and Lensky, N. G.: Sedimentology and stratigraphy of a modern halite sequence formed under Dead Sea level fall, Sedimentology, 68, 1069–1090, https://doi.org/10.1111/sed.12814, 2021.

Solari, S. and Alonso, R.: A New Methodology for Extreme Waves Analysis Based on Weather-Patterns Classification Methods, Coast. Eng. Proc., 23, https://doi.org/10.9753/icce.v35.waves.23, 2017.

Steirou, E., Gerlitz, L., Apel, H., and Merz, B.: Links between large-scale circulation patterns and streamflow in Central Europe: A review, J. Hydrol., 549, 484–500, 2017.

Syvitski, J. P. M. and Milliman, J. D.: Geology, Geography, and Humans Battle for Dominance over the Delivery of Fluvial Sediment to the Coastal Ocean, J. Geol., 115, 1–19, https://doi.org/10.1086/509246, 2007.

Syvitski, J. P. M., Kettner, A. J., Overeem, I., Hutton, E. W. H., Hannon, M. T., Brakenridge, G. R., Day, J., Vörösmarty, C., Saito, Y., Giosan, L., and Nicholls, R. J.: Sinking deltas due to human activities, Nat. Geosci., 2, 681–686, https://doi.org/10.1038/ngeo629, 2009.

Torfstein, A., Goldstein, S. L., Stein, M., and Enzel, Y.: Impacts of abrupt climate changes in the Levant from Last Glacial Dead Sea levels, Quat. Sci. Rev., 69, 1–7, https://doi.org/10.1016/j.quascirev.2013.02.015, 2013.

Torfstein, A., Goldstein, S. L., Kushnir, Y., Enzel, Y., Haug, G., and Stein, M.: Dead Sea drawdown and monsoonal impacts in the Levant during the last interglacial, Earth Planet. Sci. Lett., 412, 235–244, https://doi.org/10.1016/j.epsl.2014.12.013, 2015.

Torfstein, A. and Enzel, Y.: Dead Sea lake level changes and Levant palaeoclimate, Quat. Levant, 115–126, https://doi.org/https://doi.org/10.1017/9781316106754.013, 2017.

Tsvieli, Y. and Zangvil, A.: Synoptic climatological analysis of Red Sea Trough and non-Red Sea Trough rain situations over Israel, Adv. Geosci., 12, 137–143, https://doi.org/10.5194/adgeo-12-137-2007, 2007.

Tyrlis, E. and Lelieveld, J.: Climatology and Dynamics of the Summer Etesian Winds over the Eastern Mediterranean*, J. Atmos. Sci., 70, 3374–3396, https://doi.org/10.1175/JAS-D-13-035.1, 2013.

de Vries, A. J., Tyrlis, E., Edry, D., Krichak, S. O., Steil, B., and Lelieveld, J.: Extreme precipitation events in the Middle East: Dynamics of the Active Red Sea Trough, J. Geophys. Res. Atmos., 118, 7087–7108, https://doi.org/10.1002/jgrd.50569, 2013.

Van Hijum, E. and Pilarczyk, K. W.: Gravel beaches: equilibrium profile and longshore transport of coarse material under regular and irregular wave attack, Hydraulics laboratory, 1982.

Vüllers, J., Mayr, G. J., Corsmeier, U., and Kottmeier, C.: Characteristics and evolution of diurnal foehn events in the Dead Sea valley, Atmos. Chem. Phys., 18, 18169–18186, https://doi.org/10.5194/acp-18-18169-2018, 2018.

Wang, C., Zheng, S., Wang, P., and Hou, J.: Interactions between vegetation, water flow and sediment transport: A review, J. Hydrodyn., 27, 24–37, https://doi.org/10.1016/S1001-6058(15)60453-X, 2015.

Weisbrod, N., Yechieli, Y., Shandalov, S., and Lensky, N.: On the viscosity of natural hyper-saline solutions and its importance: The Dead Sea brines, J. Hydrol., 532, 46–51, https://doi.org/https://doi.org/10.1016/j.jhydrol.2015.11.036, 2016.

Wright, L. D.: Sediment transport and deposition at river mouths: A synthesis, Geol. Soc. Am. Bull., 88, 857, https://doi.org/10.1130/0016-7606(1977)88<857:STADAR>2.0.CO;2, 1977.

Zak, I.: The geology of Mt. Sedom, Hebrew University, 1967.

Zappa, G., Hoskins, B. J., and Shepherd, T. G.: The dependence of wintertime Mediterranean precipitation on the atmospheric circulation response to climate change, Environ. Res. Lett., 10, 104012, https://doi.org/10.1088/1748-9326/10/10/104012, 2015.

Zittis, G., Almazroui, M., Alpert, P., Ciais, P., Cramer, W., Dahdal, Y., Fnais, M., Francis, D., Hadjinicolaou, P., Howari, F., Jrrar, A., Kaskaoutis, D. G., Kulmala, M., Lazoglou, G., Mihalopoulos, N., Lin, X., Rudich, Y., Sciare, J., Stenchikov, G., Xoplaki, E., and Lelieveld, J.: Climate Change and Weather Extremes in the Eastern Mediterranean and Middle East, Rev. Geophys., 60, e2021RG000762, https://doi.org/10.1029/2021RG000762, 2022.

Ziv, B., Saaroni, H., and Alpert, P.: The factors governing the summer regime of the eastern Mediterranean, Int. J. Climatol., 24, 1859–1871, https://doi.org/10.1002/joc.1113, 2004.

Ziv, B., Harpaz, T., Saaroni, H., and Blender, R.: A new methodology for identifying daughter cyclogenesis: application for the Mediterranean Basin, Int. J. Climatol., 35, 3847–3861, https://doi.org/10.1002/joc.4250, 2015.

Ziv, B., Saaroni, H., Etkin, A., Harpaz, T., and Shendrik, L.: Formation of cyclones over the East Mediterranean within Red-Sea Troughs, Int. J. Climatol., 42, 577–596, https://doi.org/10.1002/joc.7261, 2022.

Zoccatelli, D., Marra, F., Armon, M., Rinat, Y., Smith, J. A., and Morin, E.: Contrasting rainfall-runoff characteristics of floods in desert and Mediterranean basins, Hydrol. Earth Syst. Sci., 23, 2665–2678, https://doi.org/10.5194/hess-23-2665-2019, 2019.